Engineering Geology 358 (2025) 108359

Contents lists available at ScienceDirect

Engineering Geology

journal homepage: www.elsevier.com/locate/enggeo

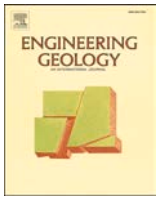

The critical role of fracture propagation in the evolution of extensive, structurally preconditioned rockslides

R. Gerstner [a,*], A. Maschler [b], B. Schneider-Muntau [c], F. Agliardi [d], M. Avian [e], M. Frießenbichler [e], C. Zangerl [a]

[a] Institute of Applied Geology, BOKU University, Vienna, Austria
[b] Department of Civil Engineering and Environmental Sciences, Western Norway University of Applied Sciences, Sogndal, Norway
[c] Departement of Infrastructure, Soil Mechanics, University of Innsbruck, Innsbruck, Austria
[d] Department of Earth and Environmental Sciences, University of Milano-Bicocca, Milan, Italy
[e] GeoSphere Austria, Department for Climate Impact Research, Vienna, Austria

ARTICLE INFO

Keywords:
High-alpine rockslides
Fractured metamorphic rock masses
Fracture propagation
Structural control
DEM/FDEM numerical modelling
Geological-geotechnical investigations

ABSTRACT

The inherited rock mass structure often preconditions rockslides in foliated, metamorphic rock slopes. However, the role of progressive fracturing processes associated with rock slope failure is receiving increasing attention. This paper demonstrates how rock mass fracturing can overcome limitations imposed by the inherited rock mass structure in two high-alpine rockslides with volumes of 670,000 and 1,000,000 m^3, applying a comprehensive methodological approach.

The rockslides' evolution and kinematics are unravelled based on remote sensing campaigns. Geological-geotechnical field and laboratory investigations provide the basis for a complementary numerical approach, utilising discrete-element (DEM) and hybrid-finite-discrete-element (FDEM) models. Leveraging the potential of each numerical approach, the rockslides are back-analysed, investigating the role of inherited structures and fracture propagation in the rockslides' evolution.

The inherited structures, particularly foliation layers and tectonic shear zones, strongly precondition both rockslides while imposing specific limitations on their initiation. Nonetheless, progressive fracture propagation overcomes these structural limitations by (i) developing a toe-breakout that provides kinematic freedom for a retrogressive rockslide on a dip-slope, and (ii) forming an active wedge in a compound rockslide, which overcomes the frictional resistance of a tectonically preconditioned basal shear zone. Furthermore, the (iii) complementary DEM-FDEM approach showcases the advantages of each respective method and reproduces these fracturing processes in remarkable agreement with field observations, holding significant implications for engineering geology and hazard assessment. Thus, this study demonstrates that even in structurally preconditioned rockslides, progressive fracture propagation can dominate over inherited structures in controlling the mechanism and evolution of large rockslides.

1. Introduction

Rock slope instabilities are common in alpine environments, particularly in heavily foliated metamorphic rock masses with a well-defined schistosity (Bunkholt et al., 2012; Zangerl et al., 2019; Vick et al., 2020; Rechberger et al., 2021), as schistosity planes significantly influence the mechanical properties of a rock by serving as preferred failure surfaces (Donath, 1961; Zhang et al., 2011). Besides the failure along schistosity planes, rock slope instabilities in metamorphic rock masses often exploit weakness zones provided by inherited, pre-existing structures, such as joints, faults, tectonic shear zones, and structures associated with folds (Agliardi et al., 2001; Brideau et al., 2009; Stead and Wolter, 2015; Agliardi et al., 2019; Zhou and Chen, 2019; Rechberger et al., 2021). In addition to the reactivation of such inherited geological structures, progressive fracturing within a rock slope can result in brittle damage accumulation and strain localization, resulting in the initiation, propagation, and coalescence of new fractures over time (Terzaghi, 1962; Eberhardt et al., 2004; Riva et al., 2018; Paronuzzi and Bolla, 2022).

* Corresponding author.
E-mail address: reinhard.gerstner@boku.ac.at (R. Gerstner).

https://doi.org/10.1016/j.enggeo.2025.108359
Received 30 January 2025; Received in revised form 15 May 2025; Accepted 15 September 2025
Available online 16 September 2025

These fractures related to progressive failure can evolve to fully persistent basal detachment surfaces for rockslides, sometimes resembling fault gouge-like materials (Chigira, 1992; Eberhardt et al., 2004; Riva et al., 2018).

Accordingly, the rupture surfaces of rockslides can often involve both pre-existing geological structures and relatively young fractures formed by progressive rock mass fracturing processes (Brideau et al., 2009; Zangerl et al., 2019). Depending on the occurrence, characteristics and orientation of pre-existing structures in relation to the slope geometry and rock mass properties, different rockslide types can be favoured (Hungr et al., 2014). A rock planar slide may develop if a single geological structure daylights on the slope at a critical dip-angle. Thereby, deformation is concentrated in a basal shear zone following a pre-existing geological structure, resulting in relatively low internal deformation of the rockslide body (Hungr et al., 2014). If the translational rock sliding mechanism exploits one or two sets of non-persistent daylighting structures, a step-path failure mechanism may form (Einstein et al., 1983) (Fig. 1a), as shown at various scales for landslides by Brideau et al. (2009).

If the structurally pre-conditioned basal shear zone – or the line of intersection of a wedge – does not daylight on the slope, kinematic freedom for rock slope failure is not provided (Havaej et al., 2013). In that case, a toe-breakout at the foot of the slope can occur, e.g., Roberts and Evans (2013), involving an active wedge and a passive wedge. In the transition zone from the active to the passive wedge, brittle rock mass fracturing must occur, including the formation of new fractures at the foot slope (Havaej et al., 2014) (Fig. 1b). If two or more geological structures form the basal shear zone, the rockslide can be termed a compound rockslide (Glastonbury and Fell, 2010). Such compound rockslides involve one or several steep fractures in the head area and a more shallow-dipping structure at the rockslide foot (Zangerl et al., 2019; Vick et al., 2020). This geometric configuration can result in the formation of an active wedge on top, driving the lower passive wedge downslope (Fig. 1c). Consequently, compound rockslides generally involve a high amount of internal deformation and shearing, especially in the transition zone from the active to the passive wedge (Glastonbury and Fell, 2010; Hungr et al., 2014).

The importance of such brittle rock mass fracturing has also prompted considerable research on the numerical representation of these processes (Elmo and Stead, 2010; Lisjak and Grasselli, 2014). These numerical models include discrete-element modelling (DEM) approaches, e.g. UDEC (Itasca, 2018) or PFC (Itasca, 2016), and hybrid finite-discrete-element models (FDEM) such as ELFEN (Rockfield, 2017) or IRAZU (Geomechanica Inc., 2024). Rock mass fracturing is regarded as a progressive, time-dependent process driven by sub-critical stress conditions, triggering localised microscopic failures, evolving to a macroscopic fracture (Atkinson, 1984; Amitrano and Helmstetter, 2006; Riva et al., 2018). When rock bridges associated with discontinuous geological structures fail, a rock mass loses cohesive elements, reducing the effective cohesion (Terzaghi, 1962). Kemeny (2005) showed, via UDEC models, that the time-dependent degradation of rock bridges, and thus the progressive rock mass fracturing, can be represented by reducing the effective cohesion related to discontinuities. Hybrid FDEM models, like IRAZU (Geomechanica Inc., 2024), are a growing alternative, as they allow to model the reactivation of pre-existing structures, as well as the progressive failure of rock bridges in a time-dependent manner (Elmo and Stead, 2010; Lisjak and Grasselli, 2014). Minor-triggering events, such as high precipitation, groundwater changes, temperature variations, or seismic activity, can be additional drivers of these progressive failure processes (Eberhardt et al., 2001; Gischig et al., 2016). Thereby, the overall rock mass strength is reduced over time, and the permeability of the rock mass is increased until the factor of safety reaches a value close to 1 (Eberhardt et al., 2001).

Besides this fracture development over geological time scales, the factor time is also expressed in high-alpine environments by rapidly changing boundary conditions, e.g. glacial retreat, changing precipitation patterns, and permafrost degradation (APCC, 2014). Since the maximum extent of the Little Ice Age (LIA) in the mid-19th century, retreating glaciers in the Alps exposed and unloaded high-alpine rock slopes (Fischer et al., 2015). These deglaciation processes can be a driver of rock slope strain localisation and timing of failure, e.g. Riva et al. (2018), also concerning the unloading effect by glacial retreat, e.g. Rechberger and Zangerl (2022). Also, several phases of glaciation and deglaciation can critically weaken a rock mass composing a rock slope (Grämiger et al., 2017). At the same time, permafrost degradation may cause changes in the hydrogeological and rock mechanical properties of a rock mass (Krautblatter et al., 2013; Sun et al., 2025).

In this paper, the combined control of inherited rock mass structure and induced rock mass fracturing on the evolution of two rockslides located on high-alpine mountain slopes of the Rauhjoch (RJ) and Mittlerer Burgstall (MB) (Fig. 2a, b) is studied. The rockslides are characterised by volumes of 670,000 (MB) and 1 million m^3 (RJ), respectively, and are located in recently deglaciated, high-alpine environments of the Eastern European Alps, slightly below 3000 m in altitude (Fig. 2c). Each of the rockslides occurred close to the boundaries of its tectonic unit (Fig. 2d), comprising highly schistose, heavily foliated poly-lithological metamorphic rock masses with inherited, pre-existing, non-persistent geological structures. Thus, they provide excellent grounds to unravel the critical role of rock mass fracturing in structurally pre-conditioned rockslides in anisotropic rock masses, demonstrating that fracture propagation can dominate over inherited rock mass structure in the evolution of two high-alpine rockslides.

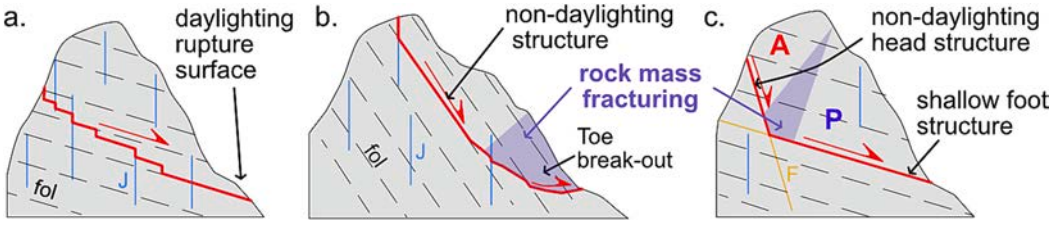

Fig. 1. Overview of rockslide types on the rock slope scale related to this paper (without claim to completeness) concerning the geometry of the basal detachment surface, based on Glastonbury and Fell (2010); Havaej et al. (2014); Hungr et al. (2014). fol … foliation; J … joint; F … fault; A … active wedge; P … passive wedge. a. Step-path failure mechanism with limited internal deformation of the rockslide; b. Non-daylighting foliation layers on a dip-slope with toe-breakout; c. Compound rockslide with active and passive wedge.

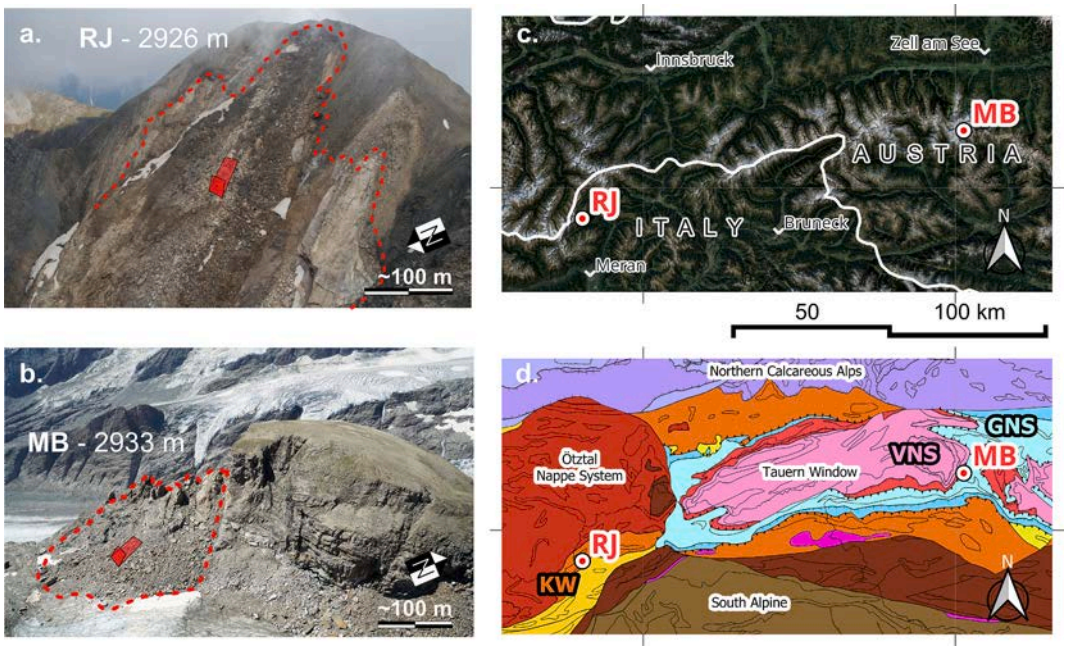

Fig. 2. Investigated rockslides. a. Rauhjoch (RJ); b. Mittlere Burgstall (MB); c. Location in the Eastern European Alps and the d. tectonic framework; map amended from ©GeoSphere Austria; KW … Koralpe-Wölz Nappe System; GNS … Glockner Nappe System; VNS … Venediger Nappe System.

2. The geological setting

2.1. Rauhjoch – RJ

The RJ rockslide lies in a complex geological setting, which has been the subject of recent regional geological research and discussion (Schmid et al., 2004; Sölva et al., 2005; Klug and Froitzheim, 2022). The geological map by GeoSphere (accessed 2025) shows that the RJ is located within the Koralpe-Wölz-Nappe system (Fig. 2d). According to the latest geological map (CARG, 2024), the RJ is situated at the southern edge of the Schneeberg Complex, bounded by the Ötztal-Stubai basement units to the north and the Texel unit to the south. Sölva et al. (2005) described the Schneeberg Normal Fault Zone as a 4.5 km thick shear zone separating the pre-alpine Ötztal-Stubai Complex from the high-pressure Texel unit. The RJ is located in this fault zone, which started to form at 95 Ma under amphibolite conditions and continued until 76 Ma under brittle conditions. Under these decreasing temperatures, strain localisation occurred, resulting in the formation of tectonic shear zones, which were active at variable temperatures and times (Sölva et al., 2005).

The Schneeberg Complex is characterised by a lithological assemblage comprising metamorphic rocks, namely marbles, calcmicaschists, amphibole- and garnet-bearing schists, and some quartzites (CARG, 2023). Marble layers occur in the rims of the Schneeberg Complex, especially at its border towards the Texel unit (Sölva et al., 2005; CARG, 2023). These rocks cropping out at the RJ exhibit a well-pronounced secondary foliation and schistosity, just as the rocks at the MB.

2.2. Mittlerer Burgstall – MB

The MB rockslide is located in the 'Hohe Tauern National Park' (Fig. 2c) in the Glockner Nappe of the Central Tauern Window (Schmid et al., 2013) (Fig. 2d). The rocks of the Glockner Nappe stem from the Penninic Valais ocean and experienced several tectonic deformation events (Schmid et al., 2013): At 45 Ma, the rocks of the Glockner Nappe were subducted below the Austro-Alpine units. The thrust of this subduction event is again folded at 35 Ma in a large-scale folding event (Schmid et al., 2013), described as a large-scale sheath fold by Groß et al. (2020), with associated fold structures occurring at the MB site. A metamorphic event which reached amphibolite facies locally is suggested to have occurred around 29 Ma, i.e. the 'Tauernkristallisation', followed by doming and lateral extrusion at around 17 Ma and rapid exhumation of the rocks of the Central Tauern Window (Schmid et al., 2013).

At the MB, Bündner-Schists (German: Bündnerschiefer) of the Glockner Nappe crop out, comprising calcmicaschists, silicate-marbles, and amphibolites (Cornelius and Clar, 1934; Höck and Pestal, 1994). They show a generally southeast-ward dipping schistosity orientation (Cornelius and Clar, 1934) and a sub-horizontal, north-northeast to south-southwest striking fold axis (Höck and Pestal, 1994). On the hardly accessible south-eastern flank of the MB, a nappe contact is indicated by Höck and Pestal (1994) and (Groß et al., 2020), showing the boundary of the Glockner Nappe System to the sub-penninic Venediger Nappe System. In Höck and Pestal (1994), these sub-penninic rocks are referred to as a 'Schuppenzone' between the Glockner Nappe and the Riffl Nappe, comprising para- and orthogneisses. Whilst the regional geological situations set the framework conditions of the RJ and the MB, geological in-situ surveys are indispensable to this study.

3. Methods

3.1. Geological- and geomechanical characterisations

Rock mass characterisation campaigns were conducted for both rockslides, comprising lithological, structural, and geotechnical investigations (Fig. 3). The lithological investigations involved geological field mapping of the outcropping lithologies at each site. To derive insights into the mineralogical content, microscopic thin-section analyses by transmissive light microscopy with a *Leica DM4500P polarisation microscope* and powder X-Ray-Diffractometry (XRD) using a *PANalytical X'Pert Pro* were conducted. The microscopic investigations further allowed us to identify microstructures within the intact rock fabric (Passchier and Trouw, 2005). The inherited rock mass structure was quantified by structural mapping on surface outcrops and — if the outcrop situation allowed — scanline recording (Priest, 1993). Six scanlines were recorded at the MB with a total length of 119.6 m. The scanlines were chosen to show variable orientations in space at each site to prevent a sampling bias due to scanline orientation. If unfeasible

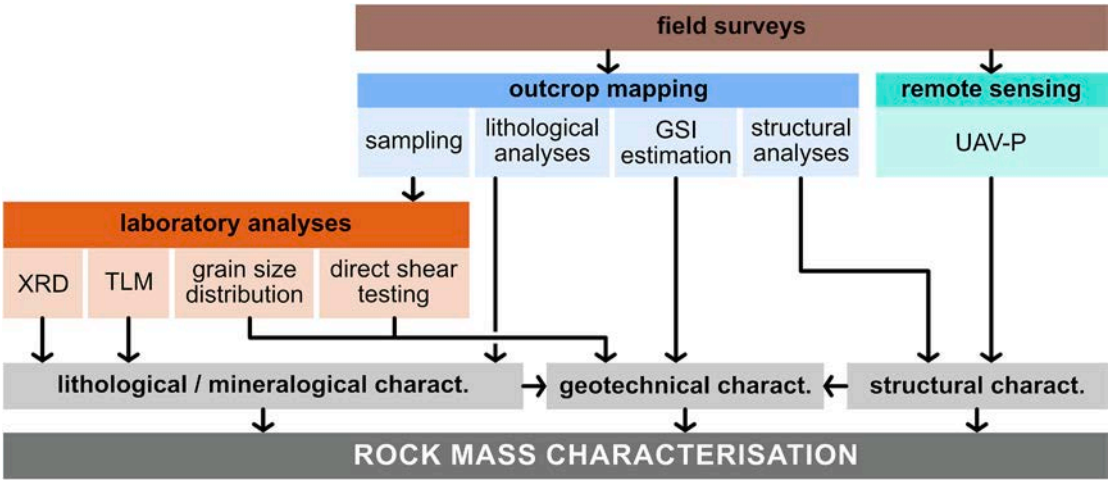

Fig. 3. Flowchart depicting the elements of rock mass characterisation conducted in this study.

conditions were encountered due to the outcrop and safety conditions at the study sites, remote structural data acquisition based on UAV-P point clouds by the CloudCompare plug-in Compass Tool (Thiele et al., 2017) provided additional data (see 3.2). Processing and graphical depiction of the structural data were done with DIPS (Rocscience, 2020). Despite the strong structural influence and anisotropic conditions at both study sites, GSI values were estimated from field observations to showcase differences in rock mass strength within the outcropping rock sequences at each site.

During the field investigation at the MB, a fine-grained, soil-like tectonic shear zone (TSZ) was identified in a surface outcrop just beside the rockslide (described in Section 4.2.3 and Fig. 12a, d). The fine-grained TSZ was regarded as potentially crucial to the rockslide development, prompting intensified mineralogical and geotechnical investigations. XRD analyses (see above) were performed on the bulk material and clay fraction. Furthermore, direct shear tests were conducted, following the standard '*ÖNORM EN ISO 17892-10:2019-04*' (extended to include cyclical application) using a 10x10x2.8 cm Wille direct shear test apparatus. To make the laboratory results more representative of the investigated scale, the shear tests were carried out on the material with a maximum grain size of 4 mm. Accordingly, the grain size distribution (D10, D30, D60, unconformity coefficient) was determined. The direct shear tests were conducted first under dry and then under fully saturated, drained conditions. The shearing process involved three loading stages with normal stress values of 100, 275 and 450 kPa for both conditions. First, the peak shear strength was determined. In the second stage, the shear strength after one cycle of shearing, i.e. 15 mm, was evaluated. Finally, the shear box was sheared multiple times (20 additional cycles) until a constant residual friction angle was achieved. A relatively slow shear velocity of 0.01 mm/min was applied to prevent pore-pressure build-up within the fine-grained sample. These shear test parameters can be found in Table 1.

3.2. Rockslide reconstruction and kinematics

The reconstruction of the rockslides' extent, features, and evolution is mostly based on orthophotos and digital terrain models (DTMs). The DTMs are derived from aerial laser scanning (ALS), unmanned-aerial vehicle photogrammetry (UAV-P), or aerial photography per plane. All data sets used in this study are listed in Table 2. To derive high-resolution 3D DTMs of the MB rockslide, UAV-P missions with real-time kinematics (RTK) were conducted at the MB, using a *DJI Phantom*

Table 1
Test parameters for the direct shear tests.

Max. grain size	Shear gap	Water content dry / fully saturated	Specimen installation unit weight	Normal stress σ	Shear displacement (1 cycle)	Shear velocity
4 mm	1 mm	0.0–0.1 / 100 %	15.7 kN/m^3	100/275/450 kPa	15 mm	0.01 mm/min

Table 2
Data used to reconstruct the rockslides; *Initial resolution was resampled for GIS analysis.

Rockslide	Purpose	Type of data, year	Source	Platform	Initial res.*
Mittlerer Burgstall MB	Pre-failure topography	DTM, 2003	(Avian et al., 2014)	Aerial photography	5 m
	Process reconstruction & kinematics, and acquisition of structural data	DTM, 2012	Land Kärnten (accessed 01/2025)	Aerial laser-scan	1 m
		DTM, 2019		UAV-P	0.1 m
		DTM, 2021	This study	UAV-P	0.1 m
		DTM, 2022		UAV-P	0.1 m
Rauhjoch RJ	Pre-failure topography	DTM, 2006	Land Tirol (2006)	Aerial laser-scan	1 m
	Process-reconstruction	Orthophotos 1945–2023	Autonome Provinz Bozen (accessed 2022)	Aerial photography	0.2–1 m
	Process-reconstruction	DTM, 2020	Autonome Provinz Bozen (accessed 2022 and processed by Maschler (2022))	Aerial photography	0.3 m
	Process reconstruction and acquisition of structural data	DTM, 2024	This study	UAV-P	0.1 m

4 and, from 2022, a *DJI Mavic 3E* (Table 2). On the RJ, a UAV-P mission with a *DJI Mavic 3E* with RTK was performed in 2024. The data was processed photogrammetrically via *Agisoft Metashape Professionell* (LLC, 2022). To analyse displacements at the MB between two DTMs, image correlation was applied on hillshades of the UAV-P-derived high-resolution terrain models (Table 2), e.g. Fey et al. (2015). A uniformly diffuse hill-shading technique on the DTMs called ambient occlusion was used, which allows for the minimisation of biases arising from different lighting directions on the DTMs (Fey et al., 2015). On these hill-shades, the *ImCORR* tool (Scambos et al., 1992) was used as a plug-in of *SAGA GIS* (Conrad et al., 2015), which has been successfully applied to various landslides (Fey and Wichmann, 2017; Zangerl et al., 2019; Gerstner et al., 2025).

For estimations of the rockslide volumes, first, the basal detachment surface of the rockslides based on the geological models was reconstructed in 3D by QGIS and the CloudCompare volume calculation tool. Then, the reconstructed pre-failure rock mass volume enveloped by these structures was calculated. The reconstructed rockslide evolutions and the rock mass characterisation campaigns provide input parameters for the numerical modelling studies and allow us to validate the model output results.

3.3. Numerical modelling

In this study, we applied two complementary 2D numerical modelling approaches in order to model rock mass fracturing: a discrete-element modelling (DEM) approach with UDEC (Itasca, 2018) and a hybrid finite-discrete modelling (FDEM) approach with IRAZU (Geomechanica Inc., 2024) (Fig. 4). The slope profile for the 2D numerical modelling studies was chosen to run parallel to the movement directions of the rock slides, coinciding with the strike of lateral release surfaces and the dip direction of basal detachment surfaces. This enabled the reduction of the 3D problem to a 2D simulation within the scope of this study. For both rockslide models, we increased the complexity of the model stepwise from isotropic-homogenous to anisotropic-heterogeneous conditions and undertook parametric sensitivity studies of the rock mechanic properties in each modelling approach.

In the DEM approach using UDEC, we implement the asymmetric Voronoi logic (Gerstner et al., 2023), applying a grain-based approach similar to the PFC, but the considered rock's micro-texture can be represented better by the usage of polygonal elements (Lisjak and Grasselli, 2014). The polygonal Voronoi tessellation was used to model such fracturing processes on the sample scale (Yan, 2008) and the slope scale (Havaej et al., 2014; Grämiger et al., 2017; Spreafico et al., 2017). Thereby, squeezed, asymmetric Voronoi elements with elongated axes allow for the schematic representation of rock mass anisotropy related to schistosity and recreate realistic fracture patterns during the initial failure of a rock slope (Gerstner et al., 2023) (Fig. 4). To represent a discontinuity network in the rock mass at a given scale of consideration, distinct, pre-existing structures can be embedded into this matrix of (relatively) small Voronoi elements (Spreafico et al., 2017).

A specific challenge in numerical approaches is scale effects (Hencher et al., 1996; Donati et al., 2021). For the Voronoi method, limitations arise if small Voronoi elements are implemented to represent 'intact rock behaviour' governed by mineralogical factors on a sub-millimetre scale, resulting in unfeasibly long computing times (Yan, 2008). As a consequence, upscaling is necessary (Gerstner et al., 2025), and rock mass or 'model properties' should be chosen for the linear elastic behaviour of the Voronoi elements (linear elastic mesh) and the Mohr-Coulomb failure criterion of the Voronoi contacts. Accordingly, the Voronoi method involves different constitutive relationships in the same model: The Voronoi elements are modelled in a simplified manner as linear elastic, isotropic elements with unit weight, Poisson ratio, and Young's modulus as input parameters. The Voronoi contacts and pre-existing structures are assigned the Mohr-Coulomb contact law, defined in UDEC by shear- and normal-stiffness, cohesion, friction angle, and a tensile cut-off (Itasca, 2018). In order to model the progressive failure within the rock mass and the loss of cohesive elements associated with increasing rock mass damage during the initial failure of the rock mass (Eberhardt et al., 2004; Kemeny, 2005; Zhou and Zhao, 2024), the Voronoi contact cohesion was reduced stepwise.

In the 2D FDEM models with IRAZU (Geomechanica Inc., 2024) an additional focus is on the development of fractures over time in interplay with glacial retreat. The rock mass is discretised into small, triangular finite elements, which are here modelled according to the linear elastic or elastoplastic constitutive relationships. The FEM material is extended to a FDEM material by the integration of four-noded cohesive crack elements (Fig. 4). These cohesive elements are assigned a cohesion,

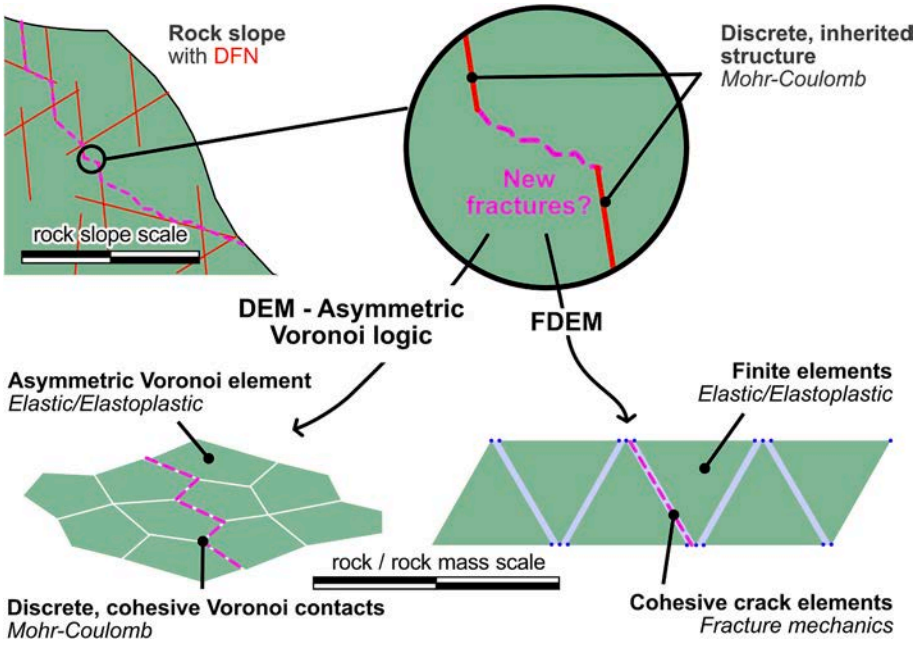

Fig. 4. Complementary DEM and FDEM approach using the asymmetric Voronoi logic (DEM) and IRAZU (FDEM) with a discrete fracture network (DFN) on the slope scale; sketch of both methods depicting the applied constitutive relationships.

friction angle, tensile strength, as well as mode I and mode II fracture energies, allowing them to develop mode I, mode II, and mixed-mode failures (Geomechanica Inc., 2024). Rock mass anisotropy is integrated into the model by assigning different strength properties to the cohesive crack elements, depending on their orientation relative to the orientation of a transversely isotropic rock mass (Geomechanica Inc., 2024). Cohesive crack elements parallel to the plane of transverse isotropy show minimum strength and increase linearly to maximum strength normal to them (Lisjak et al., 2014). As for the UDEC asymmetric Voronoi approach, the schistosity is regarded as the main rock mass anisotropy and the plane of transverse isotropy. Glacial ice was modelled for both rockslides as an elastic medium with a unit weight of 9 kN/m^3, a Young's modulus of 10 GPa, and a Poisson ratio of 0.3 (Grämiger et al., 2017; Rechberger and Zangerl, 2022). The full list of model parameters is listed with the respective modelling results in Sections 4.1.3 and 4.2.4.

The DEM (UDEC-Voronoi) and FDEM (IRAZU) approaches are used complementarily in this study. The application of UDEC especially focuses on investigating the different structural controls on the observed rockslide mechanisms in interplay with incrementally weakened Voronoi contacts. The weakening of the Voronoi contacts is conducted by reducing their effective cohesion stepwise from relatively strong to relatively weak values, thereby encouraging brittle rock mass fracturing along them. By contrast, the IRAZU approach investigates the time-dependent progressive failure of the rockslide in interaction with glacial retreat, allowing for leveraging the potential of each approach.

4. Results

4.1. The Rauhjoch RJ

4.1.1. Rockslide evolution

The RJ rockslide formed on the north-western exposed dip-slope of the 2926 m high Rauhjoch-Spitze in South Tyrol, Italy (46°49'43" N 11°06'40" E). The main scarp extends northeast-southwest with a width of circa 130 m and a length from northwest to southeast of 350 m. Maschler (2022) analysed the rockslide in detail, which developed retrogressively from the foot of the slope towards the peak in at least three stages, showing a cumulative failure volume of circa 1 million m^3. The reconstruction of the rockslide evolution by Maschler (2022) is dominantly based on the analysis of orthophotos and satellite-based photography (Table 2): A scarp-like structure is already observable on the lower part of the slope in the orthophoto of 1954, addressed as Stage 1 (Fig. 5a, b). The next detectable event occurred between June and July 2019, involving a break-off of approximately 30,000 m^3, leading to Stage 2. Stage 3 unfolded in December 2019 when a large rockslide slab of circa 950,000 m^3 detached (Maschler, 2022). As reconstructed by Maschler (2022) from Simon (1897), half of the north-western dip-slope of the RJ was covered by a glacier during the LIA, which has now disappeared completely (Fig. 5a).

In September 2021 and August 2024, extension fractures were mapped in the field on the peak area of the RJ. These extension fractures generally strike parallel to the main scarp, from northeast to southwest. The rockslide expanded laterally and retrogressively during this period, as several rock mass break-offs were found by comparing orthophotos from 2020 to 2024, resulting in Stage 4 (Figs. 5b, 6a). A strong disintegration of the rockslide mass accompanied this recent development of the RJ. While coherent rockslide slabs were still identifiable in the upper part of the rockslide in 2021 (Fig. 5a), the rockslide mass appeared as mostly incoherent rock debris in 2024. Only one slab directly below the main scarp remained distinguishable (Fig. 5b), which moved approximately 12 m to the northwest from 2020 to 2024, following the main displacement direction of the rockslide. This distinct rockslide evolution is governed by the geological conditions encountered on the RJ.

4.1.2. Geological rockslide characterisation

The RJ comprises a well-foliated, poly-lithological, fractured, metamorphic rock mass comprising calcmicaschists, marbles, as well as amphibole- and garnet-bearing schists (Fig. 6a). The calcmicaschists show well-pronounced schistosity and foliation due to muscovite and schistosity-parallel quartz layers (Fig. 6b). Biotite-rich garnet-schists crop out in the unstable rock slope's centre. Schistosity-parallel shear bands were found within these biotite-garnet-schists in the thin-section analysis. These shear bands have a thickness of up to 5 mm and are composed of angular feldspar and quartz mineral fragments of variable sizes in a fine-grained matrix. The centre of the shear band is composed of a fine-grained matrix only, imposing a pre-defined weakness zone (Fig. 6c). The amphibole-schists are mostly composed of hornblende, epidote, and up to 2 mm thick layers of biotite and chlorite (Fig. 6d).

Even on the outcrop scale, the lithological composition is often heterogeneous, with lithologies changing every few centimetres orthogonal to the schistosity planes. The strong presence of phyllosilicates – i.e., muscovite, biotite, and chlorite – within these heavily foliated lithologies results in a well-pronounced schistosity and a strong mineralogically induced transverse rock mass anisotropy (Fig. 6b, c, d). This is consistent with observations on the stable parts surrounding the rockslide, which have few in-situ outcrops due to surface coverage by a 10–20 cm thick product of physical weathering mainly composed of platy rock fragments (visible in the inlet of Fig. 5a).

These schistosity planes generally dip towards the northwest at a mean dip-angle of 37°, resulting in the dip-slope configuration (Fig. 7a) and crop out as persistent features with sizes up to 2000 m^2 (Fig. 7b). Brittle structures, such as joints, faults, and slicken-sides cross-cut the schistosity. This is visible on the microscale in Fig. 6b, where a non-

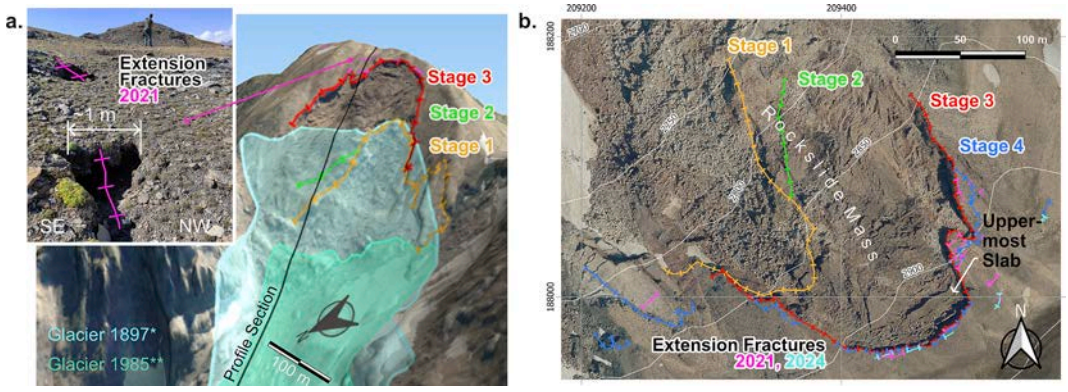

Fig. 5. The RJ rockslide a. Location in its high-alpine setting with the glacial extent 1897 reconstructed by Maschler (2022) from Simon (1897); figure inlet: Extension fracture mapped in 2021; b. Orthophoto from 2020 (Autonome Provinz Bozen, 2025) with the retrogressive development of the rockslide with the extension fractures mapped in 2021 and 2024.

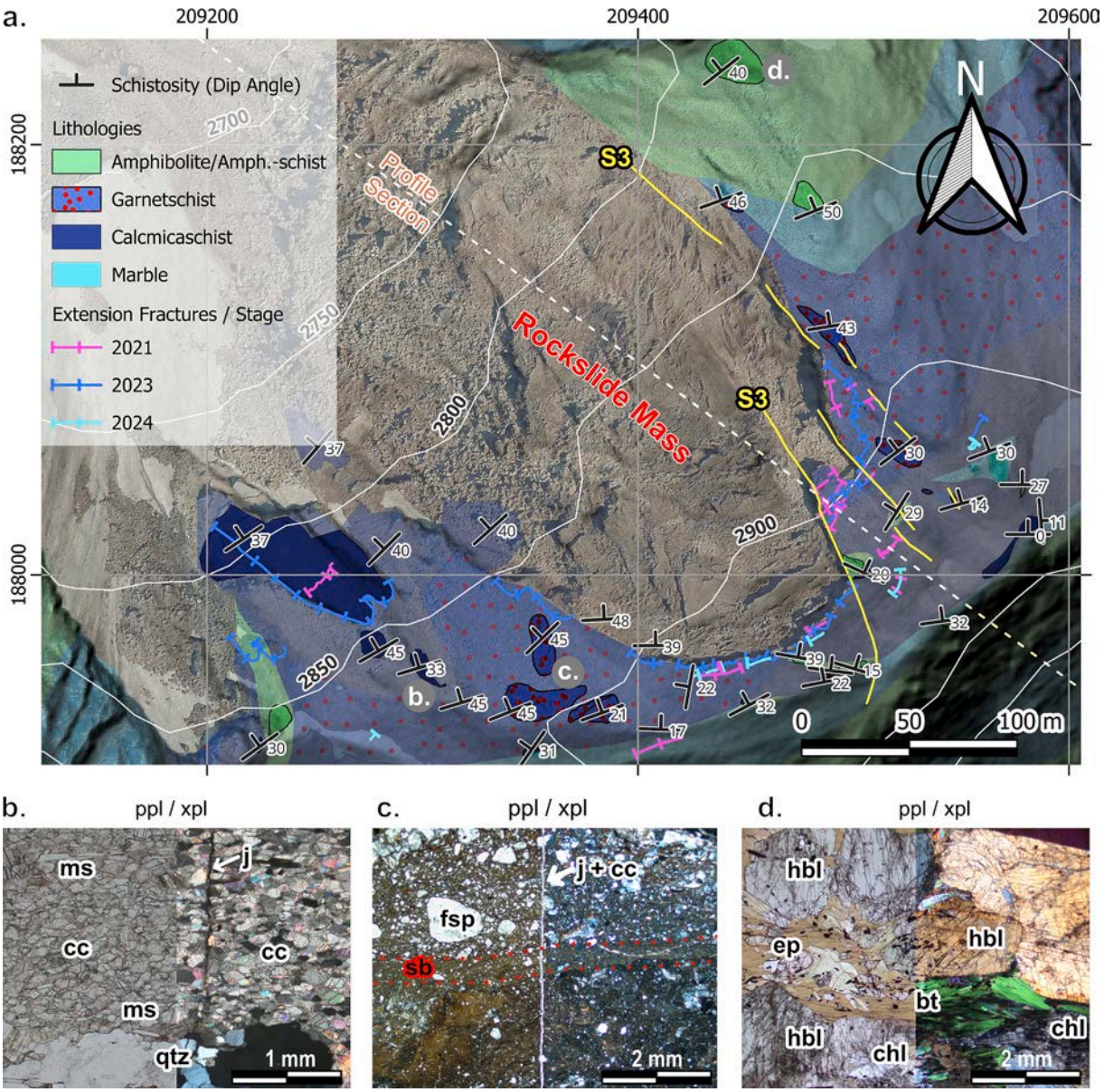

Fig. 6. Geological conditions of the RJ a. Geological map of the RJ; sampling location for thin-section analysis indicated; b. Thin-sections of calc-mica schist with a non-persistent joint (j) that terminates in a quartz-vein; main components: calcite (cc), muscovite (ms), quartz (qtz); c. Schistosity parallel shear band (sb) in a biotite-rich garnet-schist with a fine-grained matrix and angular mineral fragments of variable sizes; especially fine-grained zone in the centre; persistent joint normal to the schistosity filled with cc on the left wall (j + cc); d. Amphibole-schist with large Hornblende (hbl) crystals, epidote (ep), and mm-thick layers of biotite (bt) and chlorite (chl).

persistent joint cross-cuts the schistosity at a right angle, and in Fig. 6c, where a schistosity parallel shear band is cross-cut by a calcite-filled joint. On the outcrop scale, three sets of brittle structures, namely S1, S2, and S3, were mapped in the stable areas surrounding the rockslide and by additional remote data acquisition on the UAV-P-derived point cloud (Table 3). Sets S1 and S2 tend to be sub-vertically inclined and enclose a right angle. The S2 structures strike from northwest to southeast, i.e., sub-parallel to the rockslide's movement direction. The S1 structures are orientated orthogonally to S2 and correspond to the strike of the extension fractures formed at the peak (inlet in Fig. 5a) and with the strike of micro-structures in Fig. 6b, c. An additional set S3 is present, dipping towards the west at a dip-angle of 50°. S3 structures crop out as persistent, partly slicken-sided normal faults (Fig. 7b).

The exposed scarp area exhibits field evidence that the schistosity and the abovementioned sets S1, S2, and S3 acted as detachment surfaces and affected the geometry and failure mechanism of the rockslide (Fig. 7a, b). The persistent schistosity planes precondition the location and depth of basal detachment surfaces on the dip-slope. However, the schistosity trend is not constant and shows some deviations on the micro-, outcrop-, and slope-scale (Fig. 6a, d). At the western edge of the main scarp, the schistosity planes dip towards the north by 43°, i.e. obliquely out of the slope. They form a wedge in interplay with persistent S3 structures located at the eastern edge of the main scarp and dipping towards the west at 50° (Fig. 6a). The resulting intersection vector plunges out of the slope at 37°, i.e. the same dip-angle as the mean-schistosity orientation (Fig. 7a). Within this framework, the S2 structures act as lateral release surfaces (Fig. 7a, b), and the S1 structures provide rear detachment surfaces and were reactivated as extension fractures (inlet in Fig. 5a).

The mountain flank of the 'Imstspitze' to the southwest of the RJ offers a natural cross-section, providing an impression of the geological architecture of the RJ. In a simplified manner, we can divide the

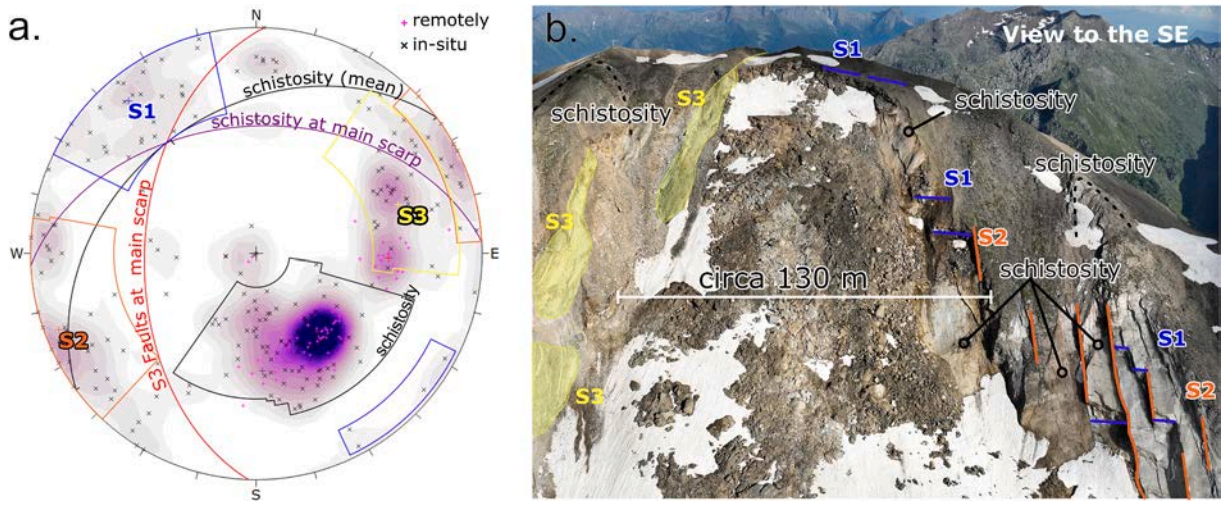

Fig. 7. Inherited structures mapped on the RJ a. Pole-plot within the equal area projection into the lower hemisphere: 294 measurements; 61 of these acquired remotely (highlighted in pink); contour scale max. density 10 %; note that the schistosity and the faults at the main scarp form a wedge with an intersection vector dipping parallel to the mean schistosity orientation; b. Main Scarp area with the structural sets indicated.

Table 3
Discontinuity sets mapped on the RJ.

Label	Mean orientation dip direction/dip angle	Number of measurements	Type(s)
Schistosity/ foliation	334/36	123	98 % schistosity planes
S1	140/77	34	91 % joints
S2	069/83	44	68 % joints
S3	251/56	42	55 % normal faults

outcropping lithologies into a weak and a strong series (Fig. 8a, b). The strong series comprises the marbles and amphibole-rich rocks. The weak series comprises intensely foliated calcmicaschists and garnet-schists (Fig. 6b) with the abovementioned shear bands parallel to the schistosity (Fig. 6c). Despite the strong structural influence on the rockslide, an estimation of the GSI reveals the difference in the respective rock mass strength of the weak (GSI 20–40, Fig. 8c) and strong series (GSI 50–70, Fig. 8d). Close to the main-scarp, the weak series crops out as a fractured, anisotropic rock mass. On the Imstspitze, a fold structure within the foliation planes is visible, characterised by shallow to sub-horizontal dip-angles of the schistosity in the peak area and steeper, constant dips in the limbs. This fold structure composed of weak and strong series layers is also visible for the RJ on the geological map (Fig. 6a), is visible at the main-scarp (Fig. 8c), can be found by the distribution of poles in the equal area projection (Fig. 7a), and is shown within the geological cross-section (Fig. 8a).

The rockslide developed within these relatively weak lithological layers of the RJ. As indicated in the profile section, it cannot be stated whether the basal sliding surface has reached the interface of the weak and strong layers. Due to the fold structure, the dip-angle of the limbs becomes steeper from the peak of the RJ towards the foot of the unstable rock slope. This implies that a possible detachment zone with a step-path geometry does not daylight on the foot of the slope (Fig. 8a).

Thus, brittle rock mass fracturing must occur in the lower part of the slope to provide kinematic freedom for rock slope failure. The numerical modelling studies investigate the development of such brittle rock mass fracturing processes, especially at the toe of the rockslide, in interplay with the pre-existing rock mass structures.

4.1.3. *Numerical modelling studies*

The pre-failure topography reconstructed by Maschler (2022) is used for the numerical studies. The slope profile for the 2D numerical studies is chosen to run parallel to the lateral release structures of S2 and the rockslide's movement direction, just as the profile section shown in Fig. 8a. In the numerical studies, various sets of rock mass properties were taken from tunnelling data and tested in over 50 modelling series. The best results were achieved by assigning relatively low friction angles of 22° to the rock mass, representing heavily anisotropic, heterogeneous, intensely foliated, schistose rocks (Table 4). These properties are considered adequate, considering the well-pronounced schistosity and schistosity-parallel shear bands (Fig. 6b, c).

We integrate the pre-existing rock mass structure into the final DEM Voronoi model (UDEC), including the folded weak and strong lithological sequences (Fig. 8a, b, c, d). Furthermore, the folded schistosity planes are integrated as discrete, persistent fractures. Then, the weak series is tessellated into a matrix of small, asymmetric Voronoi elements, which are inclined according to the mean dip-angle of the schistosity (i.e., 37°). Finally, non-persistent, brittle structures related to the S1 set are implemented into the matrix of small, asymmetric Voronoi elements (Fig. 9a). Except for the Voronoi contact cohesion, the properties assigned to these structures were held constant for the six series presented herein and can be found in Table 4. The effective Voronoi contact cohesion was successively decreased from 0.5 MPa (1st series) to 0.0 MPa (6th series), thereby encouraging brittle rock mass fracturing and resembling the time-dependent degradation of rock bridges (Table 4).

In the 1st series, presented in Fig. 9b, the Voronoi contacts were assigned relatively strong properties, i.e., a cohesion of 0.5 MPa, thereby subduing brittle fracturing along them. The friction angle of the Voronoi contacts and the shear strength properties of the folded foliation planes and the S1 structures were held constant according to the parameters listed in Table 4. No rock slope failure was observed in this 1st series (Fig. 9b).

Then, the cohesion of the Voronoi contacts was reduced stepwise. In the 5th series, at a cohesion of 0.1 MPa for the Voronoi contacts, failure occurred at the foot of the slope (Fig. 9c). Subsequently, the rockslide developed retrogressively, exploiting the elongated axis of the Voronoi contacts and the pre-existing structures related to the persistent foliation planes and S1. The rockslide did not fail as a single, coherent slab. In turn, it showed several break-offs, starting at the toe of the slope,

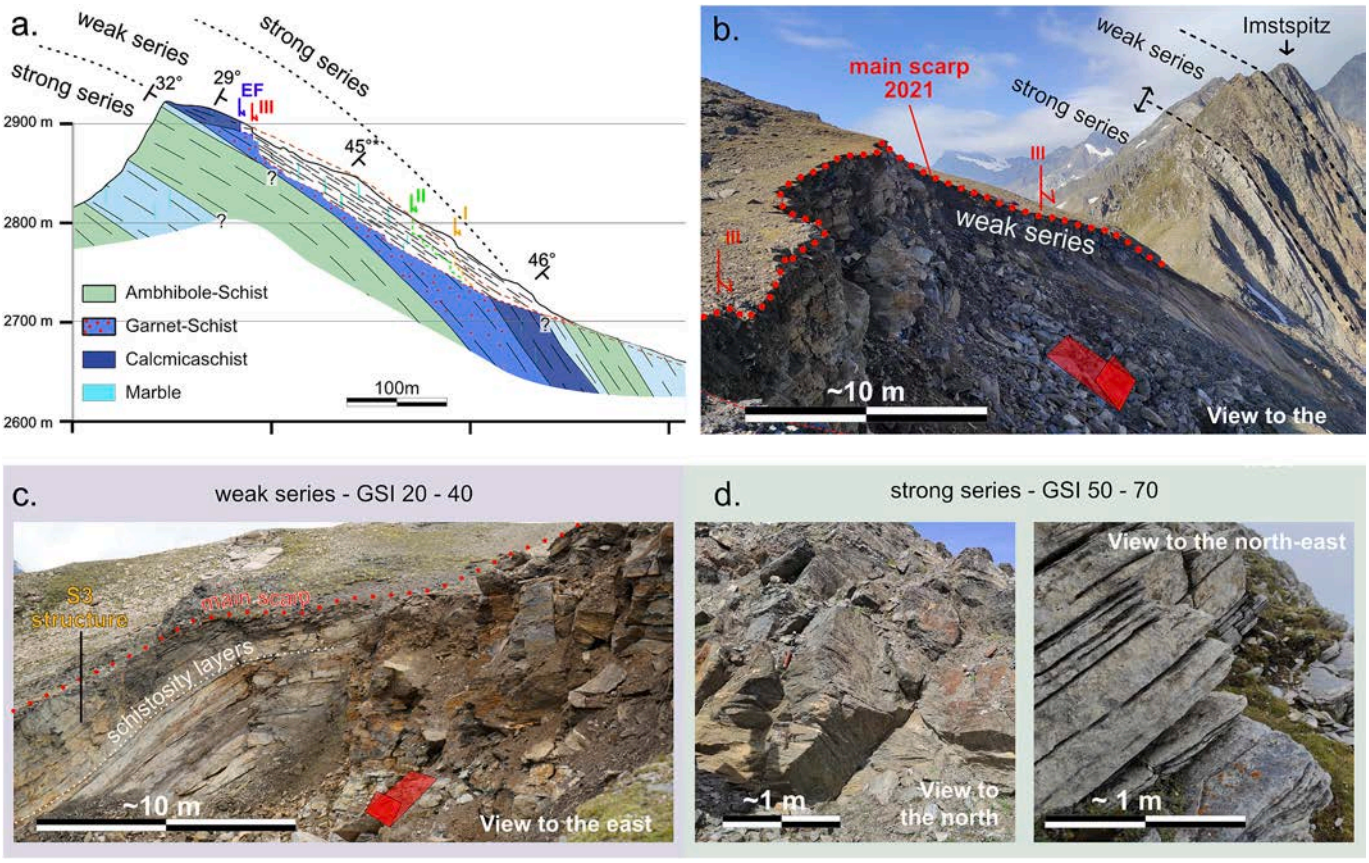

Fig. 8. Geological rockslide model of the RJ; a. Geological profile section parallel to S2 with the weak and strong series indicated; b. View to the west over the main scarp towards the Imstspitz, providing a natural cross-section; c. Sequence of garnet-bearing schists and calcmicaschists at the main scarp allocated to the weak series with estimated range of GSI values; d. Compact amphibole schists (at the base of Imstspitz) and homogeneous marbles (south of the main-scarp) allocated to the strong series with estimated GSI values on the outcrop scale.

Table 4
Input parameters for the UDEC model for the RJ presented herein.

Rock mechanic entity constitutive relation	Property, Abbr.	Series conducted						Unit	Explanation
		1st	2nd	3rd	4th	5th	6th		
Voronoi contacts & Discrete schistosity planes; Mohr-Coulomb	*Cohesion, c*	5e5	4e5	3e5	2e5	1e5	0	[Pa]	
	Friction angle, φ			22				[°]	
	Tensile cut-off, t	2.5e5	2e5	1.5e5	1e5	5e4	0	[Pa]	
Voronoi elements; Linear-Elastic	*Unit weight, γ*			25.5				$\left[\frac{kN}{m^3}\right]$	*from unpublished tunnelling data in heavily anisotropic, heterogeneous, intensely foliated, schistose rocks*
	Young's modulus, E			20e9				[*Pa*]	
	Poisson ratio, ν			0.2				[ ]	
Joint-sets S1, S3; Mohr-Coulomb	*Cohesion, c*			0				[Pa]	
	Friction angle, φ			22				[°]	

representing a toe-breakout. This toe-breakout provided kinematic freedom for the successive failures developing retrogressively towards the peak, with each slab showing a deeper detachment horizon. The displacement rates of the slabs decreased upwards, reaching almost zero at the peak, where the schistosity dips at a shallower dip-angle. Only some S1 structures were reactivated in the peak area, representing the extension fractures mapped in the field (compare Fig. 5a, b). Further decreasing the cohesion to 0 MPa resulted in a stronger disintegration of the rockslide body until a contact overlap limit stopped the modelling procedure. The toe-breakout is crucial for forming the rockslide. In the UDEC Voronoi model, it developed at the foot slope of the RJ without any prior assumptions of the location of rock slope failure, just as suggested in the geological model (Fig. 7a).

An additional modelling approach on the same slope profile using the FDEM approach with IRAZU investigates how these fractures develop over time, including six glacial stages (Fig. 10a). Rock mass anisotropy is integrated into the weak lithological layer by assigning minimum and maximum strength properties – comprising cohesion, tensile strength, and Mode I and II fracture energy – to the cohesive bands depending on their orientation in a ratio of 1:5 (Table 5, Fig. 10b).

By removing the glacial stages 1 and 2, the first fractures formed in the rock slope at the interface between the strong and the weak

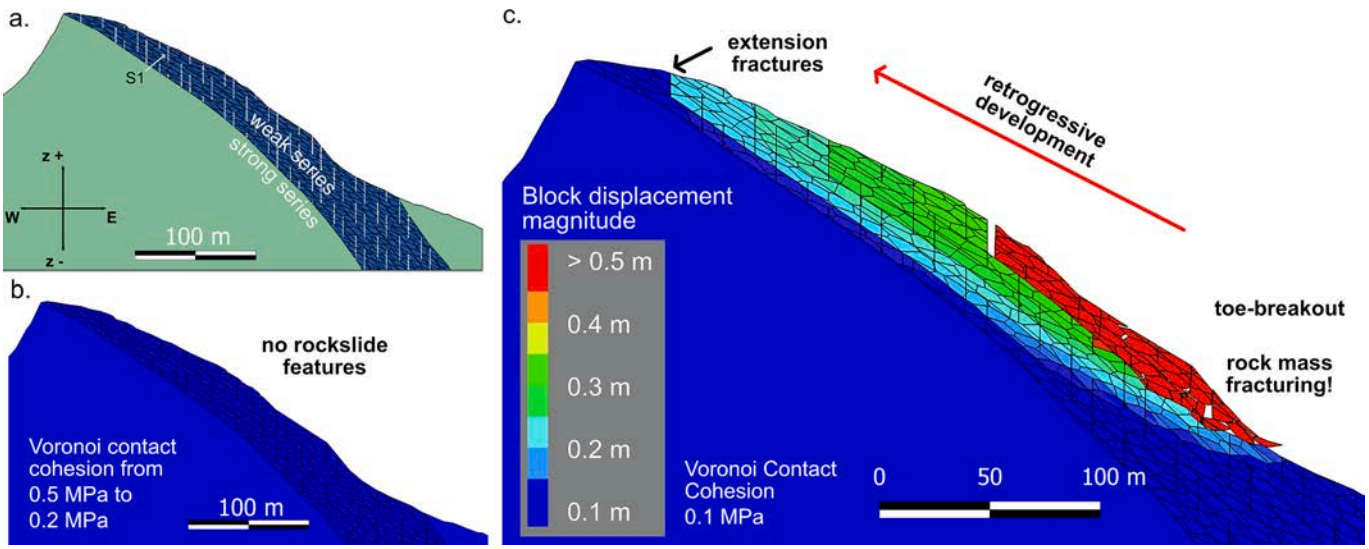

Fig. 9. DEM studies on the RJ; a. Model set-up according to the slope profile in Fig. 8a; b. 1st modelling series with brittle rock mass fracturing subdued at a cohesion for the Voronoi contacts of 0.5–0.2 MPa (same colour scale as for Fig. 5c); and c. 5th modelling series with the cohesion reduced to 0.1 MPa for the Voronoi contacts.

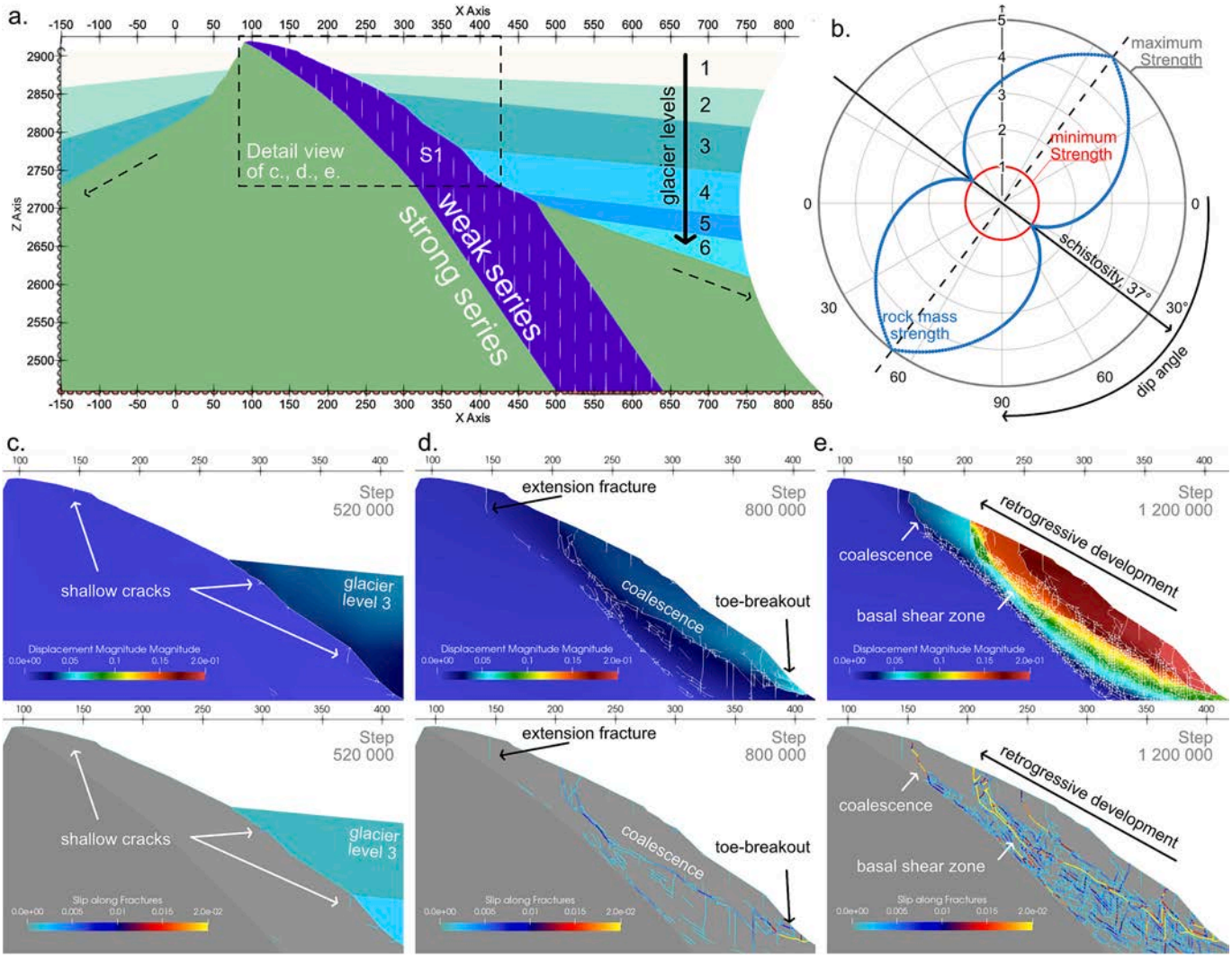

Fig. 10. FDEM model of the RJ using IRAZU a. Model set-up (compare Fig. 9a), the slopes are extended gently; b. Strength of the cohesive bands dependent on their dip-angle in relation to the dip-angle of the schistosity; c. First cracks after removing the first glacial stage; d. Increased fracture density and propagation upwards; d. Fracture accumulation & first complete coalescence; e. Extension fractures forming and development of the toe-breakout.

Table 5
Input parameters for the weak series in the IRAZU model for the RJ presented herein.

Entity constitutive relation	Property, symbol, unit	Min/max	Source/explanation
	Friction angle, φ, [°]	22	see above
	Cohesion, c, [Pa]	8e4 / 4e5	
	Tensile strength, t, [Pa]	4e4 / 2e5	Ratio of minimum to maximum strength (anisotropy): 1:5
	Mode I fracture energy, GI, [N/m]	2.8 / 3.2	
Cohesive bands	Mode II fracture energy, GII, [N/m]	28 / 32	Relation from Whittaker et al. (1992) in Geomechanica Inc. (2024)
	Young's modulus, E, [Pa]	25e9	
	Poisson ratio, ν, [ ]	0.25	
	Unit weight, γ, [kN/m^3]	2600	
	Friction angle, φ, [°]	22	
	Cohesion, c, [Pa]	8e3	
Finite elements *Elastoplastic*	Tensile strength, t, [Pa]	4e3	see above
	Friction angle, φ, [°]	26	
	Cohesion, c, [Pa]	8e4	
	Tensile strength, t, [Pa]	4e4	
	Mode I fracture energy, GI, [N/m]	2.8	
Pre-existing structures	Mode II fracture energy, GII, [N/m]	28	assumptions

lithological layer and in shallow depths (Fig. 10c). Some shallow cracks formed on the foot slope at the same spot where the toe-breakout occurred in the UDEC model (Figs. 9c, 10c). Further reducing the glacial level, now only covering the foot slope of the RJ, resulted in increased fracture density. Removing the last glacier remnants from the slope led to the coalescence of the fractures, delineating a large rockslide slab but with limited displacement (Fig. 10d). Also, the toe-breakout formed, and an extension fracture opened close to the peak of the RJ. This coalescence of the basal detachment surface of the large slab was followed by a rapid increase in displacement (Fig. 10e).

At 800,000 steps, the displacement is mostly concentrated in a distinct basal shear zone (Fig. 10d). This is consistent with field observations of the main scarp area, where planar, persistent schistosity planes crop out (Fig. 7b). With increasing displacement, the basal detachment horizon fans out into a broader zone of fractures, but the rockslide slabs remain less fractured (Fig. 10e). Still, looking at the slip along the fractures, the first persistent basal detachment surface that formed (Fig. 10d) is identifiable with increased displacement, as most of the slip is concentrated in this zone (Fig. 10e).

An additional FDEM model series studied the effect of glacial retreat. Although deglaciation to the approximate level of 1897 initiated some cracking at the foot slope, no coalescence of the fractures developed. Thus, brittle rock mass fracturing linked to glacial retreat on the RJ proved crucial in forming a toe-breakout. After this first failure occurred, a retrogressive rockslide developed in the model, reproducing all diagnostic rockslide features of the RJ observed in the field in two independent numerical modelling approaches using both DEM and FDEM techniques.

4.2. The Mittlerer Burgstall MB

4.2.1. Rockslide evolution

The MB is a 2933 m high northwest-to-southeast trending, glacially shaped ridge in a high-alpine environment. The ridge is characterised by a 280 m wide, dome-like plateau in the northwest and narrows to only a few meters in the southeast. While the plateau slopes gently towards the Pasterze glacier in the north, it shows two steep to sub-vertical flanks to the northeast and southwest (Fig. 11a). The MB resembled a nunatak during the maximum extent of the Pasterze Glacier in the LIA as it was enveloped by a small glacial tongue of the Pasterze on its north-eastern slope and by the main tongue of the Pasterze on its south-western slope (Kellerer-Pirklbauer et al., 2012). Detailed paintings from the 1830s depict the MB as a nunatak during the LIA, showing that half of the north-eastern ridge was covered by the smaller but topographically higher tongue of the Pasterze glacier, whilst the glacial tongue on the south-western slope was already substantially lower. Since this situation at the end of the LIA, these glacial levels decreased significantly by ~70 m on the north-eastern and by ~250 m on the southwestern slope (Kellerer-Pirklbauer et al., 2012).

Following an extraordinarily warm winter, significant rock slope instability processes occurred at the MB in the spring and summer of 2007, causing a fundamental change to the shape of the narrow south-eastern section of the ridge (Kellerer-Pirklbauer et al., 2012). The rock debris mobilised in these events deposited on the ridge and both flanks, whilst some relatively intact rock towers remained within the mass (Fig. 11a). Fig. 11a shows a reconstruction of the pre-failure topography based on the DTM of 2003 and the UAV-P-derived DTM from 2020 (Table 2), highlighting how dramatically the shape of the mountain

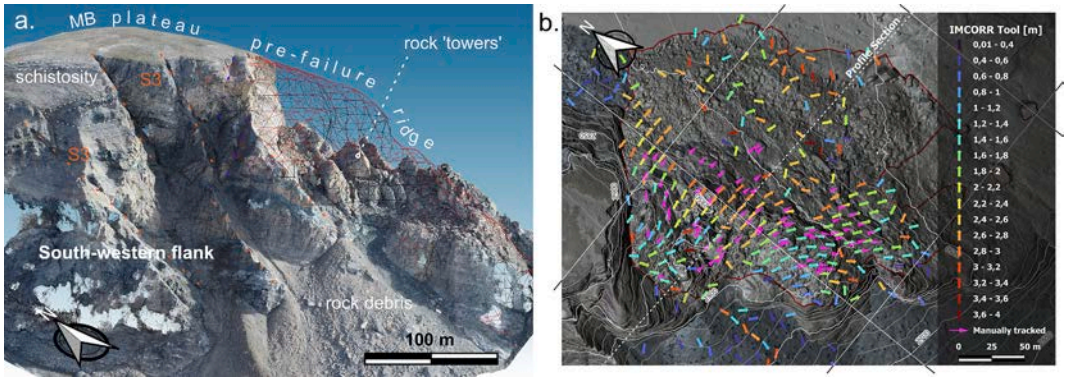

Fig. 11. Overview of the MB a. MB Pre-failure topography based on the 2003 DTM (Avian et al., 2014) and the UAV-P derived DTM from 2020; b. Ongoing displacements of the MB rockslide revealed by feature tracking by IMCORR derived between the DTMs of 2019 and 2022 (Table 2), showing the eastwards-directed movement of the rockslide body.

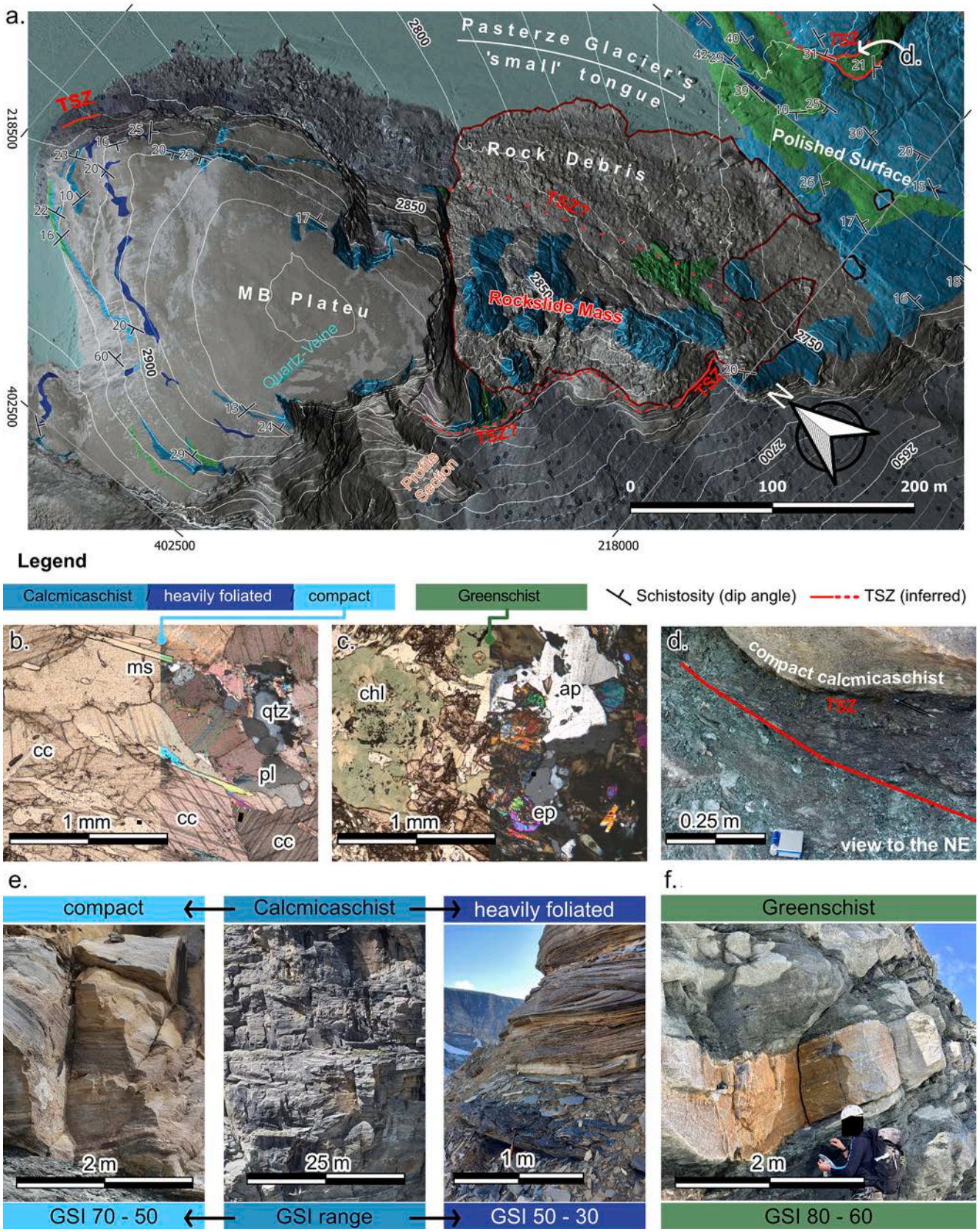

Fig. 12. Geological conditions of the MB a. Geological map of the MB; Greenschist rocks and a tectonic shear zone (TSZ) can be traced around the base of the MB and on the glacially polished surface; hill-shade based on the DTM of 2022 (see Table 2) b. Thin-section analysis in plane-polarized light (left) and crossed polarized lights (right) of a b. compact calcmicaschist (cc … calcite, ms … muscovite, qtz … quartz, pl … plagioclase) and a c. greenschist (chl … chlorite, ap … apatite, ep … epidote); d. TSZ at the interface between compact calcmicaschist (on top) and the greenschist rocks, location of the sampling is indicated by 'd.' in Fig. 11a; e. Estimated ranges of GSI values on the outcrop-scale for the calcmicaschists; f. Compact greenschist with an intercalated band of compact calcmicaschists.

flank was altered.

The initial rock slope failure in 2007 prompted regular surveillance campaigns starting in 2010, which were conducted annually using TLS (from 2010 to 2019) and UAV-P (ongoing since 2019). These studies revealed that the entire south-eastern ridge of the MB, involving a volume of approximately 670,000 m^3, displaced eastward by approximately 2.2 m in the period of 2019 to 2022 (Fig. 11b).

This eastward-directed movement involved the complete unstable section of the south-eastern ridge, including the relatively intact rock towers cropping out of the rock debris, indicating that a rock sliding mechanism is the underlying process of rock slope instability (Fig. 11a). The rock slope instability of the MB, its movement direction, and its kinematical behaviour are controlled by the geological conditions of the MB.

4.2.2. Geological rockslide characterisation

The MB is dominantly composed of calcmicaschists (Fig. 12a, b). The intensity of the schistosity in the calcmicaschists varies from compact, silicate-marble-like rocks to heavily foliated, mica-schist-like horizons (Fig. 12e). Compact greenschist rocks are intercalated into these calcmicaschists (Fig. 12c, f). These greenschists follow the general schistosity trend and can be traced around the base of the MB on the geological map (Fig. 12a) and on the UAV-P model (Fig. 11a) and are characterised by a paragenesis of chlorite, apatite, amphibole minerals, and epidote (Fig. 12c). The lithologies strike along the general schistosity trend, which is not constant, showing slight deviations along an east-west trending great circle, suggesting a fold structure with a north-south trending sub-horizontal fold axis. Besides folds, large-scale boudin structures are present. The boudins consist of competent, green-schist boudin elements within a matrix of relatively incompetent calcmicaschists, causing additional local undulations of the schistosity orientation (Fig. 11a).

As revealed by scanline recording, brittle joints and faults crosscut the schistosity and the lithological series. These structures can be categorised into three sets (Table 6). Two sub-vertical sets, S1 and S2, strike east-west and north-south, respectively, enclosing a right angle and following the regional joint pattern (Fig. 13b). The retreating small tongue of the Pasterze glacier on the north-eastern slope exposed a polished surface just east of the unstable rockslide mass, offering an excellent outcrop situation (Fig. 12a). In this section, lineaments of the east-west striking set S2 are identifiable, showing that these structures crop out as highly persistent features, while the S1 joints show limited persistence. Additional structural data on the inaccessible rupture surface was acquired from the high-resolution UAV-P-derived DTMs (Table 2). These structures can be attributed to a highly persistent east-southeast-ward-dipping set S3 (Fig. 13b), comprising persistent structures that are part of a conjugate system, also visible on the south-western flank of the MB (Fig. 11a).

At the interface between the greenschist and the calcmicaschists, a schistosity-parallel, fine-grained, soil-like tectonic shear zone (TSZ) with a thickness varying from a few cm to over 1 m was identified (Fig. 12d). This TSZ is also identifiable on the 3D drone model at the interface between calcmicaschists and greenschists at the base of the rockslide mass, showing a high-persistence and planar geometry (Fig. 12a). As shown in the geological profile section, a connection between the greenschist rocks mapped on the MB and the greenschist rocks on the polished surface is reasonable (Fig. 13a). This implies that the TSZ daylights on the north-eastern slope of the MB somewhere under the rock debris (Fig. 12a), with a maximum daylighting dip-angle of 15°. This maximum dip-angle is considered herein (Fig. 13a, b).

In the southern part of the rockslide, the TSZ undercuts the complete rockslide mass, suggesting that the rockslide moves along the predestined horizon in a translational rock-sliding mechanism. In the northern part of the rockslide, the detachment zone is more complex, involving steeper structures associated with S3 at the head of the rockslide, forming a compound rock-sliding mechanism (Fig. 13a, c). The compound rock sliding mechanism involves an active wedge, separated from the stable areas by the steep S3 structures, and a passive wedge, sliding along the pre-destined basal detachment horizon provided by the TSZ. A zone of intense fragmentation developed between the active and the passive wedge, as visible on the 3D UAV-P point cloud (Fig. 13c). This is also supported by the surface displacements between the DTMs of 2003, 2012, and 2022, indicating that the displacement of the active wedge is steep to sub-vertical, whilst the passive wedge displaces at more shallow dip-angles (Fig. 13d). However, the compound rockslide mechanism shown in Fig. 13 requires a low friction angle of the TSZ, prompting intensified studies on the TSZ material, resembling a soil-like, fine-grained material.

4.2.3. Rockslide shear zone characterisation

By XRD, the mineralogy of the soil-like, fine-grained TSZ material on both the bulk material and the clay fraction was determined. The results on the bulk material revealed that the main components of the material are chlorite and amphibole minerals, with talc as a subordinate component. The same minerals were found in the clay fraction. The grain size distribution for the material <4 mm revealed a d10 value of 14 μm, a d30 value of 132 μm, and a d60 value of 800 μm, and thus a coefficient of curvature C_c of 1.6. To determine the shear strength parameters of the TSZ material, direct shear tests were conducted (test set-up see 3.1), once in dry conditions and once fully saturated (Fig. 14a,b). For both conditions, the linearised shear strength properties at their peak strength of the first shearing cycle, at the end of the first shearing cycle (15 mm shear distance), and the residual shear strength after additional 20 cycles (315 mm) are presented.

A reduction of the shear strength of the dry TSZ material was identified in the normal stress range for the shearing apparatus, i.e. 100 kPa to 500 kPa, for both dry and wet conditions with increasing shear distance (Fig. 14a). The shear strength reduction under dry conditions is mostly due to a decrease in cohesion from a peak value of 47 kPa to 33 kPa after the first shearing cycle to a residual value of 23 kPa. The cohesion is sensitive to the shear distance on the sample, but the friction angle stayed relatively constant at 23 to 24° (Fig. 14c). Under wet conditions, the failure envelope further decreased for the investigated range of normal stresses (Fig. 14b). In contrast to the dry conditions, the shear strength reduction is due to a reduction of the friction angle from 24° (peak) to 17° (1st cycle/residual). The friction angle decreased with increased shearing distance, but the cohesion increased from 8 kPa (peak) to 17 kPa (residual) under wet conditions. By contrast to the dry conditions, the residual value was almost reached after the 1st cycle of shearing.

The lowest friction angle achieved for the material, which was under wet, residual conditions, involves a friction angle of 17°. This value is still higher than the maximum dip-angle of the TSZ zone (15°) derived in the geological profile section (Fig. 13a). However, as presented in Fig. 13a, the basal detachment horizon involves the TSZ at the foot of the rockslide and steeper S3 structures at the head, forming a compound rockslide architecture with an active and a passive wedge. Also, the higher dip-angle of the S3 structures (~60°) increases the overall dip-angle of the basal detachment surface from ~15° to ~23°. However,

Table 6
Discontinuity sets mapped on the MB.

Label	Mean orientation dip direction/dip angle	Number of measurements	Type(s)
Schistosity/ foliation	093/15	137	95 % schistosity planes and the tectonic shear zone
S1	284/86	69	77 % joints
S2	004/84	130	88 % joints
S3	122/56	42	74 % joints, 17 % faults

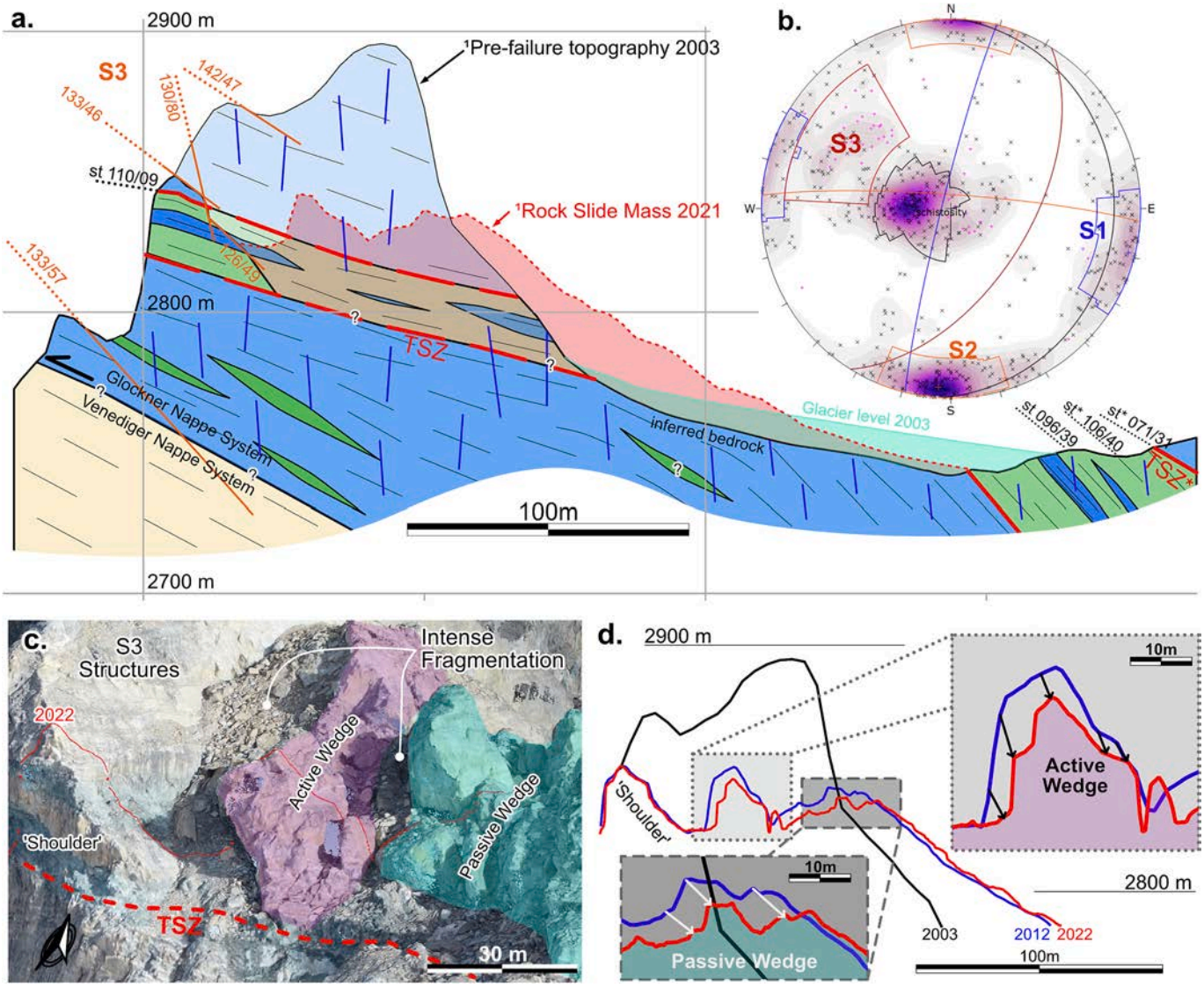

Fig. 13. Geological rockslide model of the MB; a. Profile section parallel to the lateral release surface of S2; Legend see Fig. 12; [1]DTM source see Table 2; b. Inherited structures as a pole-plot within the equal area projection into the lower hemisphere: 605 measurements; 70 of these acquired remotely (highlighted in pink); contour scale max density 10 %; c. RGB point-cloud of the MB with the profile section '2022' indicated; active and passive wedge indicated; d. Detailed view of the DTMs 2003, 2012, and 2022 (see Table 2) and the displacements observed with steep displacement vectors (active wedge) and more shallow vectors (passive wedge).

brittle rock mass fracturing must occur in the transition zone from the driving to the passive wedge to accommodate the compound rockslide geometry and to transmit the driving force imposed by the active wedge. The combined control of these structures and brittle rock mass fracturing is investigated within the numerical investigations.

4.2.4. Numerical modelling studies

For the numerical studies, the pre-failure topography (Avian et al. (2014), Table 2) is used (Fig. 15a). The 2D numerical studies on the MB involve the slope profile parallel to the lateral release surface of the highly persistent S2 structures (Fig. 12a) and the geological profile section (Fig. 13). The model further considers the lithological and structural conditions by integrating the calcmicaschists with the intercalated greenschists, the TSZ, and the brittle structures associated with S1 and S3. Furthermore, rock mass anisotropy related to schistosity is integrated into the model in the same manner as described for the RJ (see 4.1.3). For the DEM Voronoi approach, the main schistosity orientation is represented by the elongated Voronoi axis, here dipping towards the east by 13° (to the right in Fig. 15a). As for the RJ, several parametric studies were conducted for the MB. The input parameters for the final UDEC modelling series are listed in Table 7, with Voronoi contact cohesion values varying in eight different series between 5 and 0 MPa. For each of these eight series, six different properties of the TSZ were tested according to the results of the direct shear tests (Fig. 14). These involved a consecutive reduction of the shear strength properties of the TSZ from peak to residual properties first under dry conditions and then under wet conditions. The friction angle was further reduced to 15° and finally to 8° only. This results in 48 modelling scenarios (Table 7).

In the 1st series, with a relatively strong Voronoi contacts cohesion of 5 MPa, no failure was initiated at the MB, even by assigning the wet, residual conditions to the TSZ. The first minor displacements along the TSZ were recorded when a friction angle of 15° was applied to the TSZ, which equals its dip-angle (Figs. 13a, 15a). Further reducing the friction angle to 8°, i.e. way below the lowest laboratory value for wet residual conditions of 17°, resulted in the first considerable displacements on the MB in this 1st series. However, the S3 structures were not reactivated, and no strong internal fragmentation of the rock mass was observed, as the displacement was confined along the TSZ, resulting in a translational rock sliding mechanism (Fig. 15b).

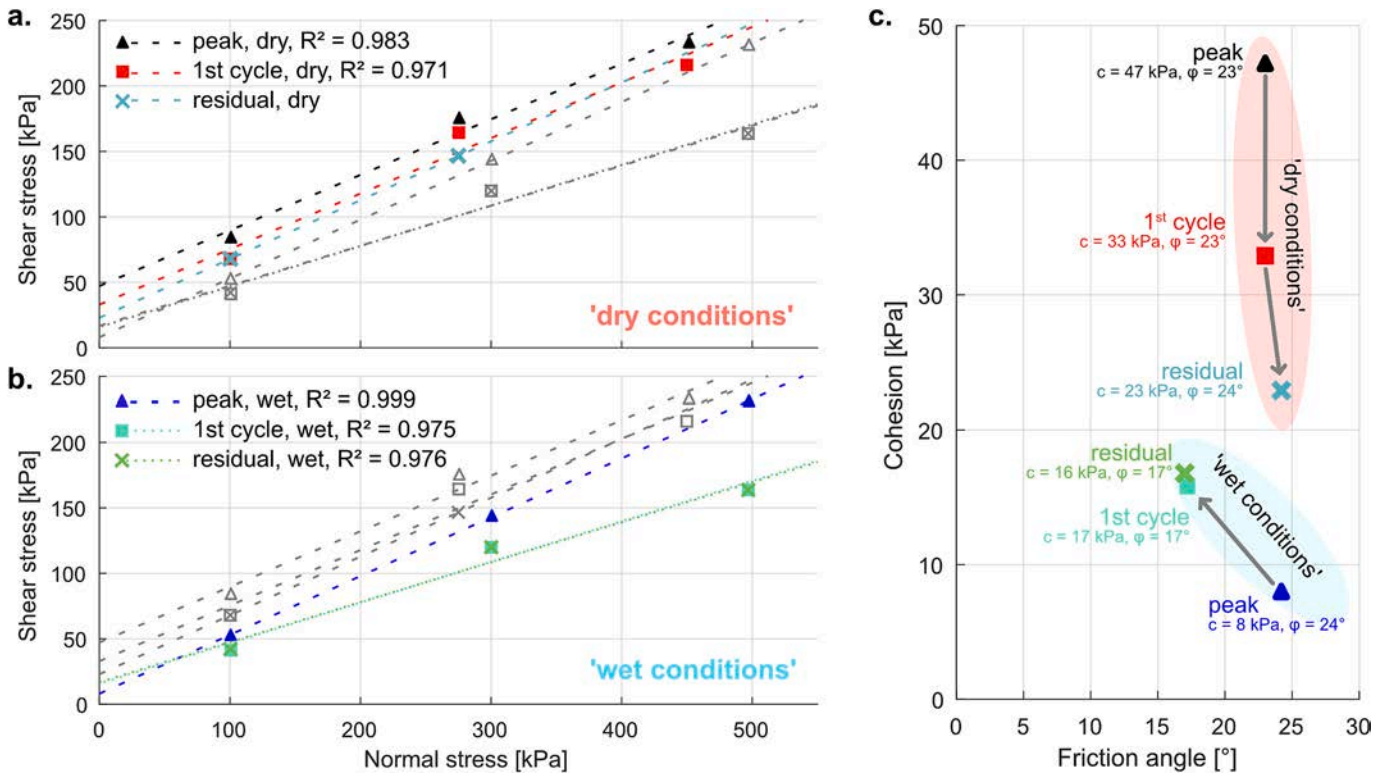

Fig. 14. Linearized results on the shear strength of the TSZ material showing the peak shear strength, the shear strength after one shearing cycle and the residual shear strength after several cycling procedures for a. Dry conditions; b. Wet conditions; c. Comparison of the development of friction angle and cohesion for all testing procedures.

Starting from a Voronoi contact cohesion of 0.5 MPa (5th series), some rock slope failure processes initiated already under dry, residual conditions for the TSZ. These included the reactivation of the S3 structures and the formation of wing cracks originating from the tips of pre-existing S1 structures in the centre of the slope, located above the intersection between the S3 structures and the TSZ. In the 7th series, at 0.1 MPa Voronoi contact cohesion, the fracture paths propagated further from these wing cracks and coalesced with shallow fractures (Fig. 15c). However, no reactivation of the TSZ was observed.

Finally, wet, residual conditions for the TSZ, i.e. $\varphi = 17°$; $c = 17$ kPa, resulted in the reactivation of the TSZ and the shallow cracks coalesced and became more abundant in a zone of fracturing (Fig. 15d), delineating an active wedge from a passive wedge. The passive wedge moved in a translational rock sliding mechanism along the TSZ, whilst the active wedge moved downwards in a rotational-like movement (Fig. 15d), reproducing the compound rockslide mechanism addressed before (Fig. 13a, c, d). However, a rock bridge located above the intersection of the S3 structures with the TSZ remained (Fig. 15d), showing a shear-stress concentration of the elastic Voronoi elements up to 8 MPa (Fig. 15e). In the next step, elastoplastic properties were assigned to the Voronoi elements (the same elastoplastic properties as for the finite elements in the IRAZU FDEM approach found in Table 8). The stress concentration in Fig. 15e resulted in increased strain rates in the rock bridge area and in the transition zone between the active and the passive wedge, causing larger rockslide displacements (Fig. 15f). After this increase in displacements due to elastoplastic Voronoi element behaviour, the rockslide stabilised again.

An additional hybrid FDEM approach by IRAZU investigates the formation of cracks over time in interaction with glacial retreat since the LIA maximum extent in the MB area. The model set-up included the same pre-existing structures as presented for the UDEC model, but without the Voronoi elements. Instead, finite elements with elastoplastic behaviour were implemented, bounded by cohesive bands (Table 8, Fig. 4). Rock mass anisotropy due to schistosity was included in the same manner as for the RJ (compare Fig. 10b), with a dip-angle of 13° for the weakest cohesive elements. The in-situ stress state was initialised with a glacial level covering almost the complete eastern side of the MB, resembling the situation at the LIA (see 4.2.1).

Under dry conditions of the TSZ ($\varphi = 24°$, $c = 23$ kPa), some fractures formed in the area east of the S3 structures with the glacier still in place. No rock slope failure was initiated, even under dry residual conditions and by completely removing the glacier. Then, the wet residual conditions were assigned to the TSZ, i.e., $\varphi = 17°$, $c = 17$ kPa. Again, fractures formed even with the glacier still in place (Fig. 16a), similar to those observed for the dry conditions. These included wing cracks originating from the tips of pre-existing S1 structures in the same manner as observed for the DEM studies (Fig. 15c). In shallow regions of the MB, the wing cracks propagated from the S1 structures upwards and reached the surface (Fig. 16a, x 45, z 2870), similar to those observed in the DEM studies in Fig. 15d. Also, the TSZ was reactivated at the foot of the MB. Despite the formation of these fractures, the MB remained stable. Another fractured zone formed on the steep western flank of the MB (x -10, z 2800).

Removing the last bit of glacial ice from the foot of the MB resulted in a daylighting TSZ, which was completely reactivated, accompanied by a rapid increase in fracture density between x-coordinates 10 to 50 (Fig. 16b). Also, the displacement increased, showing a vertical downward movement just east of the S3 structures (x 20, z 2860). Moreover, the S1 structures coalesced almost vertically at $x = 50$, with only small rock bridges remaining (Fig. 16b, x 50, z 2825), already delineating the future active wedge. This resembled similar conditions as observed for the DEM Voronoi studies in Fig. 15d.

The failure of the rock bridges followed immediately, and a 5 to 10 m thick fractured zone developed in the same zone ($x = 50$), where the first coalescence was found (Fig. 16c). The fractured zone now fully delineates the active wedge (displacement vectors parallel to the two S3

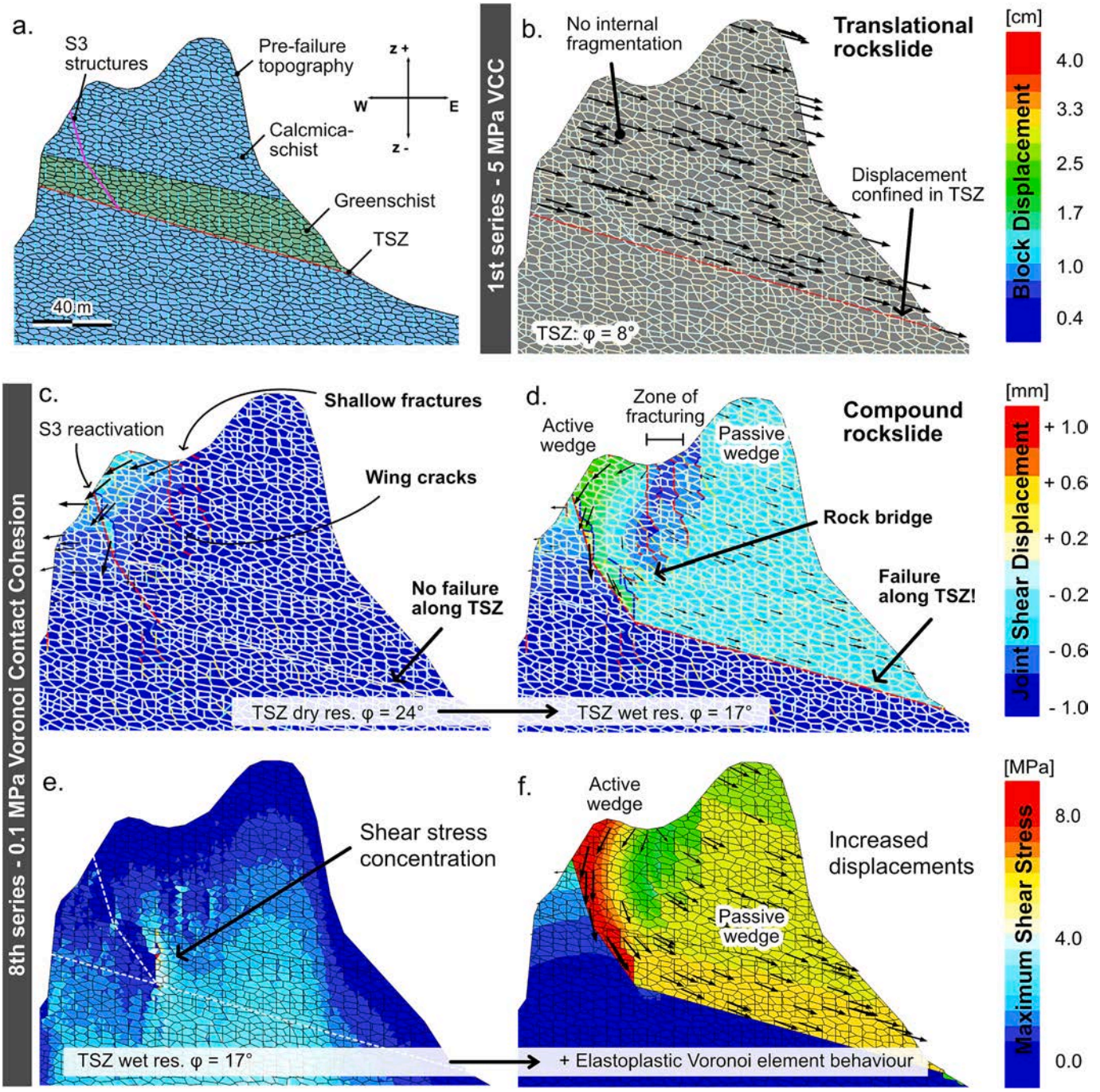

Fig. 15. MB DEM (UDEC asymmetric Voronoi) studies a. Model set-up with lithological boundaries, TSZ, and inherited structures (S1 and S3; input parameters in Table 7); b. 1st series – strong Voronoi Contact cohesion (VCC, 5 MPa); complete translational rockslide at $\varphi = 8°$; 7th modelling series with 0.1 MPa VCC with; c. Dry, residual conditions for the TSZ; reactivation of the S3 structures and formation of shallow cracks; d. Wet residual conditions for the TSZ; reactivation of the TSZ and S3 structures; compound rockslide; rock bridge remaining with; e. Stress concentration in this rock bridge section; f. Elastoplastic behaviour showing increased displacements of the rockslide.

Table 7
Input parameters for the DEM of the MB; Parameters presented in *Fig. 15b, **Fig. 15c, ***Fig. 15d, e; φ = friction angle; c = cohesion; t = tensile cut-off.

Constitutive relation	Condition / property	Modelling series								Unit	Explanation
		1st	2nd	3rd	4th	5th	6th	7th	8th		
Voronoi contacts Mohr-Coulomb	*c*	5e6	1e6	0.5e6	0.4e6	0.3e6	0.2e6	0.1e6	0e6	[Pa]	
	φ	30°	30°	30°	30°	30°	30°	30°	30°	[°]	*reduced stepwise*
	t	2.5e6	0.5e6	0.25e6	0.2e6	0.15e6	0.1e6	0.05e6	0e6	[Pa]	
TSZ Mohr-Coulomb	*dry, peak / φ; c*	23; 47e3	23; 47e3	23; 47e3	23; 47e3	23; 47e3	23; 47e3	23; 47e3	23; 47e3	[°]; [Pa]	*see* Fig. 14
	dry, res./ φ; c	24; 23e3	24; 23e3	24; 23e3	24; 23e3	24; 23e3	24; 23e3	**24; 23e3****	24; 23e3		
	wet, peak / φ; c	24; 8e3	24; 8e3	24; 8e3	24; 8e3	24; 8e3	24; 8e3	24; 8e3	24; 8e3		
	wet, res. / φ; c	17; 17e3	17; 17e3	17; 17e3	17; 17e3	17; 17e3	17; 17e3	**17; 17e3*****	17; 17e3		
	additional runs / φ; c	15; 0 **8; 0***	15; 0 8; 0	15; 0 8; 0	15; 0 8; 0	15; 0 8; 0	15; 0 8; 0	15; 0 8; 0	15; 0 8; 0		
Voronoi elements Linear-Elastic	*Unit weight γ*	25.5 / 28.5								$\left[\frac{kN}{m^3}\right]$	*Calcmica−/ Green-Schist; From unpublished tunnelling data;*
	Y.'s modulus E	36e9 / 43e9								[*Pa*]	
	Poisson ratio ν	0.29 / 0.26								[ ]	
Joint-Sets S1, S3 Mohr-Coulomb	*c*	0								[Pa]	
	φ	26								[°]	/
	t	*0*								[Pa]	

structures) from the passive wedge (displacement vectors parallel to the TSZ). Moreover, a disintegration of the active wedge is observable, where the two S3 structures intersect, resulting in the formation of an additional, small active wedge (x 25, z 2835). At the same time, the 'shoulder' delineated by the S3 structures remained stable. Then, the model displacement increased further, and the offset of the active wedge became visible (Fig. 16d). Although the displacement increased, the fragmentation was still mostly concentrated in the transition area between the active and the passive wedge, whilst the passive wedge remained relatively unfractured.

In the combined DEM and FDEM approach, it was possible to show that brittle rock mass fracturing is crucial in forming an active wedge that results in the overall increase of the dip-angle of the basal detachment surface, allowing it to overcome the shear resistance provided by the TSZ. Also, this rock mass fracturing is strongly linked to the presence and orientation of pre-existing structures of tectonic origin, i.e. the steeper S3 structures and the TSZ. These pre-existing structures form the structural predisposition for a compound rock sliding mechanism. The dip-angle and shear strength of the TSZ proved to be the most critical parameters in the parametric studies. As the shear strength of the TSZ is sensitive to water content, water may have played an important role in the rockslide evolution, which is discussed in 5.2.

5. Discussion

5.1. Interplay between inherited structures and rockslide-related rock mass fracturing (RJ)

The structurally preconditioned basal detachment surface of the RJ rockslide provided by the schistosity planes does not daylight on the slope (Fig. 8a). This results in stable conditions in a simple kinematic analysis (Wyllie and Mah, 2004), as the foliation layers find an abutment in the slope, e.g., Havaej et al. (2014). In the case of the RJ, this constraint imposed by the inherited structures and the topography is overcome by rock mass fracturing in the form of a toe-breakout. Thereby, the overall dip-angle of the basal detachment surface is reduced and reaches the daylight envelope, providing the kinematic freedom for rock slope failure (Fig. 17a). This is well exemplified by the DEM-Voronoi models, where rock slope failure only initiates and progresses if brittle rock mass fracturing is allowed, triggering the toe-breakout (Fig. 9c). This was reproduced in the same location and geometry in the FDEM model (Fig. 10d).

Table 8
Model input parameters for the weak series in the IRAZU model for the MB presented herein.

Entity constitutive relation	Property, symbol, unit	Greenschist min/ max	Calcmicaschist min/ max	Source/explanation
Cohesive bands	Friction angle, *φ, [°]*	30	30	see above
	Cohesion, c, [Pa]	4e5 / 2e6	1.5e5 / 7.5e5	
	Tensile strength, t, [Pa]	2e5 / 1e6	7.5e4 / 3.8e5	Ratio of minimum to maximum strength (anisotropy): 1:5
	Mode I fracture energy, GI, [N/m]	3 / 5	3.5 / 4.5	
	Mode II fracture energy, GII, [N/m]	30 / 50	35 / 45	Relation from Whittaker et al. (1992) in Geomechanica Inc. (2024)
	Young's modulus, E, [Pa]	25e9	20e9	
	Poisson ratio, ν, [ ]	0.26	0.29	
	Unit weight, γ, [kN/m^3]	28.5	25.5	
Finite elements *Elastoplastic* TSZ	Friction angle, *φ, [°]*	30	30	
	Cohesion, c, [Pa]	6e5	4e5	
	Tensile strength, t, [Pa]	3e5	2e5	assumptions
	Dry, residual; *φ [°]; c [Pa]*	24; 23e3		
	Wet, residual; *φ [°]; c [Pa]*	17; 17e3		two individual runs
Pre-existing structures	Friction angle, *φ, [°]*	26		
	Cohesion, c, [Pa]	0		
	Tensile strength, t, [Pa]	0		assumptions

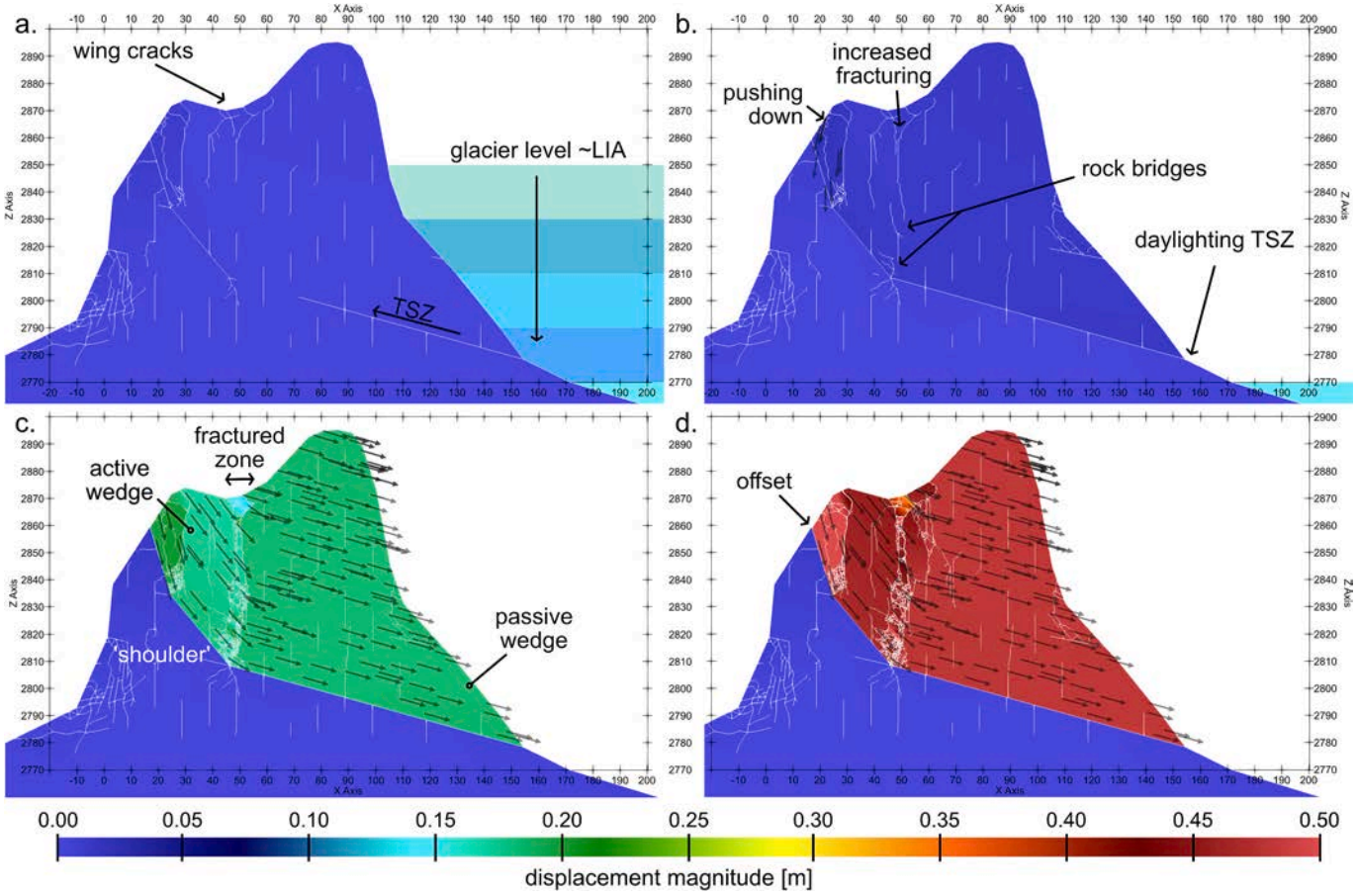

Fig. 16. FDEM model of the MB using IRAZU with wet, residual conditions assigned to the TSZ; a. 60,000 steps; b. 260,000 steps; c. 680,000 steps; d. 1,000,000 steps.

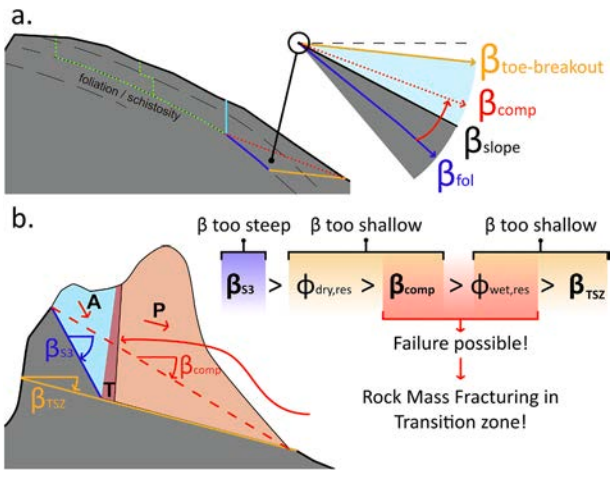

Fig. 17. Geometrical and geotechnical situations of the rockslides; a. RJ: The decrease of the dip-angle of the basal detachment zone to reach the daylight envelope on the foot of the RJ; b. MB: The increase in the dip-angle of the basal detachment zone to overcome the shear resistance of the TSZ.

The FDEM studies further showed that the retreating glacier was crucial in initiating the rockslide (Figs. 10c to e). A correlation between glacial retreat and rock slope failure has been found in many studies (Grämiger et al., 2017; Riva et al., 2018; Rechberger and Zangerl, 2022). In the case of the RJ, the glacier's stabilising effect may have been twofold. First, the glacier, which still covered half of the slope in 1897 (Fig. 5a), provided a load on the RJ's foot, hindering the formation of a toe-breakout. Second, the removal of the glacial ice must have caused a stress redistribution in the rock mass, potentially causing the formation of new fractures and the reactivation and propagation of pre-existing structures (Grämiger et al., 2017). Thereby, rock mass permeability was most probably increased, and water would have been more abundant within the rock slope (Riva et al., 2018), potentially saturating the schistosity parallel shear bands found in the thin-section analysis (Fig. 6c). This correlates with the findings of Maschler (2022), who showed that the large 2019 event on the RJ (leading to stage 3, Fig. 5c) was initiated after heavy snowfalls and a subsequent increase in temperature, followed by the rapid melting of the snow cover. Thus, the retreating glacier may have been one factor that increased the susceptibility to failure of the RJ over time. Removing the last glacial ice from the toe slope of the RJ in the FDEM model runs resulted in the coalescence of fractures, providing a fully persistent basal detachment surface leading towards the toe-breakout (Fig. 10d). After the toe-breakout, the retrogressive rockslide development unfolded in the UDEC investigations, just as observed in nature (compare Figs. 9c to 5a,b). Also, the extension fractures mapped around the peak in the summers of 2021 and 2024 were reproduced numerically.

Whilst rock mass fracturing is crucial for the RJ, it is still preconditioned by the lithological conditions and inherited rock mass structure. Also, in both numerical approaches, the geometry and depth of the basal detachment zone were only reproducible by introducing the weak and strong lithological series (Figs. 9a, 10a). Furthermore, the highly persistent schistosity planes act as pre-defined basal detachment horizons, especially in the upper and central part of the rock slope (Fig. 7b). Also, the retrogressive rockslide development did not involve the peak,

where the fold structure on the RJ results in more shallow dipping foliation planes. Moreover, brittle structures such as faults, joints, and slickensides assignable to three sets act as lateral release surfaces and provide the predisposition for this distinct rockslide development.

5.2. Active wedge formation in a compound rockslide (MB)

The rock slope instability on the MB is strongly linked to tectonic structures, i.e. the tectonic shear zone (TSZ) and the steep S3 structures at the head of the rockslide (Fig. 13a), forming the compound rockslide architecture (Glastonbury and Fell, 2010; Vick et al., 2020). This was reproduced in both numerical approaches – DEM (Fig. 15d) and FDEM (Fig. 16d) – where an active wedge was formed, sliding down the reactivated S3 structures. The active wedge provides a force on the passive wedge, which then moves along the deformation horizon provided by the TSZ in a translational rock sliding mechanism (Fig. 13a, d). Consequently, the shear strength properties of both the S3 structures and the TSZ are crucial for the process development, whereby the numerical investigations showed that the shear strength of the TSZ is far more sensitive to the process. The residual friction values for the TSZ material show $\varphi_{dry,res} = 24^\circ$ and $\varphi_{wet,res} = 17^\circ$ for dry and wet conditions, respectively. In comparison, Strauhal et al. (2017) and Agliardi et al. (2020) found residual friction angles ranging from 19° to 28° for fault gouges associated with rockslides in foliated metamorphic rock characterised by a high quantity of phyllosilicates. At the same time, the formation of the active wedge resulted in an overall increase of the dip-angle of the basal detachment surface, combining the S3 structures with a dip-angle of circa $\beta_{S3} \approx 60^\circ$ with the TSZ with a dip-angle $\beta_{TSZ} \approx 15^\circ$ to a compound dip-angle of $\beta_{compound} \approx 23^\circ$. As the S3 structures alone dip too steeply (non-daylighting structures), and the TSZ dips too shallowly (frictional resistance too high), the compound rock sliding mechanism is the only combination where failure can occur (Fig. 17b).

The Voronoi approach reproduced the initial rockslide geometry in good agreement with field observations and the FDEM results. However, after short displacements, the rockslide stabilised again. While the Voronoi approach allows the representation of rock mass anisotropy in the initial development of the rockslide (Gerstner et al., 2023), the distinct Voronoi shape hindered the free development during larger displacements, especially in the transition zone between the active and the passive wedge (Fig. 15d). This, in turn, shows how critical this brittle rock mass fracturing is in the compound rockslide architecture of the MB. Furthermore, the Voronoi elements impose asperities on newly formed detachment zones. This may be representative of natural rock slope failures, where a blocky rock mass also imposes asperities. However, whilst these blocky portions of the rock mass may break in nature if a certain stress value is overcome, the Voronoi elements can only deform in an elastic or elastoplastic manner. This is one of the key advantages of the FDEM approach (Elmo and Stead, 2010; Lisjak and Grasselli, 2014). In the FDEM model of the MB, such a progressive fracturing concentrated in distinct zones in the rock mass was observed in the transition zone between the active and passive wedge: A 5–10 m thick zone of fractured rock formed, while the rest of the rockslide remained relatively intact (Fig. 16d). These observations fit well with the intact rock towers cropping out of the rockslide mass in nature (Fig. 11a).

As reproduced in both modelling scenarios, the wet residual shear strength properties for the TSZ derived in the direct shear tests (i.e., $\varphi = 17^\circ$) are capable of accommodating the compound rock sliding mechanism, but only if rock mass fracturing is allowed (either by weak Voronoi contacts in the DEM approach or by the FDEM approach). If rock mass fracturing is hindered (strong Voronoi contacts), a shear strength of the TSZ way below the laboratory values (i.e., $\varphi = 8^\circ$) is necessary to reproduce significant displacements in the UDEC modelling scenarios presented herein. Also, the observed rock slope failure under these extraordinary low shear strength conditions was a complete translational rock sliding mechanism, not representative of the failure mechanism observed in nature (Fig. 15b). However, assuming the dry, residual conditions (i.e., $\varphi = 24^\circ$) resulted in some localised fracturing on the slope, but no final rock slope failure occurred in either of the modelling scenarios. Thus, only the combination of wet-residual conditions of the TSZ and the compound rockslide constellation was feasible in reproducing the compound MB rockslide.

Such a reduction of the shear strength due to saturation is most likely due to the mineralogical content of the TSZ, including chlorite and talc (Fig. 14c). This may give us an important hint regarding the final trigger of the rockslide. Besides water from precipitation, water may be supplied to the MB by the melting glacier, which surrounds the ridge from three sides. This water could migrate along the schistosity planes and reach the TSZ. It is safe to assume that the permeability of the rock mass has increased in recent decades by two processes: On the one hand, permafrost degradation is known to increase rock mass permeability, e.g. by removing the ice filling of joints (Pogrebiskii and Chernyshev, 1977; Krautblatter et al., 2013). On the other hand, several glaciation and deglaciation phases – as experienced by the MB (Kellerer-Pirklbauer et al., 2012) – increased the number of cracks and the coalescence of the discontinuity network, further increasing its permeability (Grämiger et al., 2017). These mechanisms may result in a positive feedback loop, potentially favouring the development of a perched aquifer on top of the (relatively) impermeable TSZ (Riva et al., 2018; Agliardi et al., 2020).

5.3. Implications for numerical modelling and hazard assessment

The MB and the RJ are located in remote, high-alpine settings. In both cases, mountain huts lie close to the rockslides. The Seeberalm mountain hut lies circa 5 km 'downstream' from the RJ's main scarp with a mean slope gradient of 11°. Fahrböschungs angles smaller than 11° have been reported in the literature, however, such low values are only expected for rockslide volumes larger than 10^7 m^3. Even if the simultaneous mobilisation of the entire rockslide volume of 10^6 m^3 (Maschler, 2022) is assumed, a Fahrböschung angle of 11° is not to be expected according to the published data. Also, a complete mobilisation of the rockslide is considered unlikely due to the strong disintegration of the rockslide mass. However, this strong disintegration results in a high availability of sediments. Intense rainfall or snow-melting events may trigger debris flows that could potentially reach the Seeber Alm in a cascade event. Prochaska et al. (2008) present field data of several debris flow events with Fahrböschung angles ranging from 23° to 7°, but usually, these debris flows show runout lengths below 1 km.

The strong disintegration of the RJ rockslide mass further implies that monitoring individual slabs is hardly possible, and measured surface velocities are not representative of the overall displacement of the rockslide mass. Still, information on the near-surface displacements may be critical for the extension fractures mapped around the RJ peak, as a hiking path runs sub-parallel to the strike of the main scarp. The fractures became more frequent from 2021 to 2024, suggesting that the rockslide development is not finished. Extensometers would provide a well-established tool to monitor the aperture of the fractures, allowing to close the hiking trail if increased displacements are measured. Also, it can be expected that more water can infiltrate deeper sections of the rock slope through these extension fractures, further saturating the schistosity parallel shear bands. At the same time, a stabilising effect may arise from the shallower dip-angles of the schistosity planes observed at the peak due to the fold structure (Fig. 13a).

No hiking path crosses the MB or the deposition zone of the rockslide mass. Still, the adjoining mountain of the 'Hohe Burgstall' resembles similar geological conditions and morphology as the MB and houses the Oberwalder Hütte, which is one of the main alpine training centres (Kellerer-Pirklbauer et al., 2012). However, as the distinct TSZ was crucial in the MB rockslide formation, the stability of the Hohe Burgstall must be assessed separately from that at the MB. Still, regular field investigations and in-situ monitoring of ongoing processes, next to the established UAV-based monitoring system at Hoher Burgstall, are recommended for early detection of rock slope instabilities. A similar

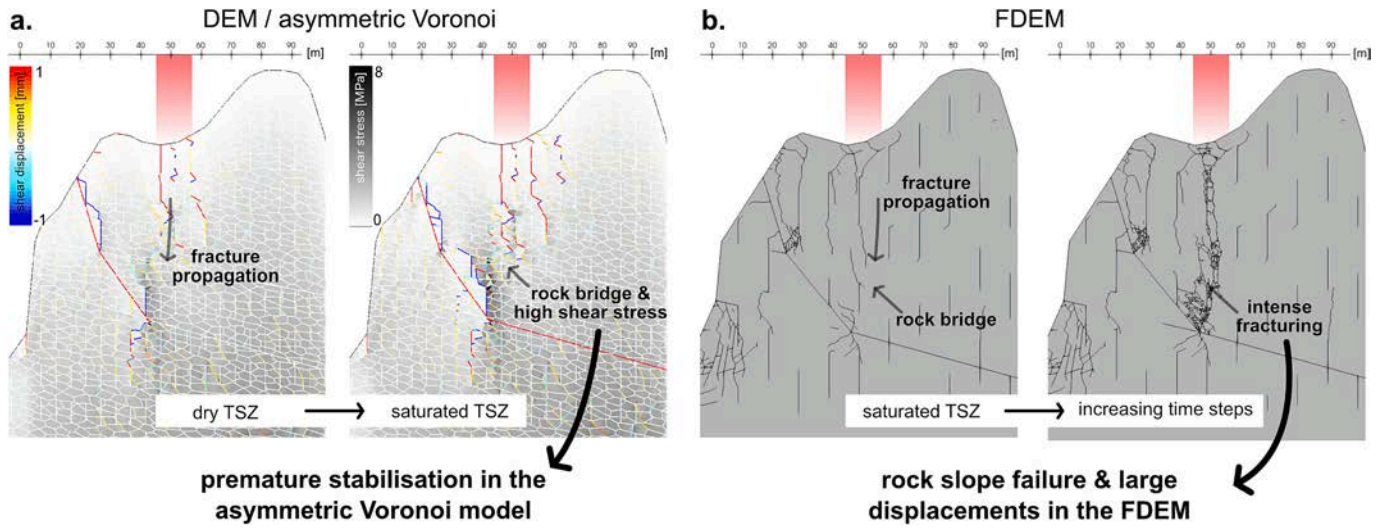

Fig. 18. Comparison of the complementary DEM-FDEM approach. a. DEM/asymmetric Voronoi model (8th series, compare Fig. 14); left: dry, residual friction angle for the TSZ, fractured zone initiates as wing cracks and fractures propagate downwards; right: saturated, residual friction angle for the TSZ. Fractured zone propagates, rock bridge with high shear stresses remains; b. FDEM model at saturated, residual friction angle for the TSZ with increasing time steps from left to right figure; fracture propagation initiates and evolves to a fully persistent zone of intense fracturing.

system as for the MB, comprising UAV-P surveys (and historically TLS measurements) in combination with geological-geotechnical investigations, is likely to be the most feasible combination to detect a potential rock slope instability and characterise ongoing processes on the Hohe Burgstall.

The compound rockslide model identified for the MB further carries important implications for hazard assessment: Even if the friction angle of a critical tectonic shear zone (residual friction angle of 17° under fully saturated conditions) exceeds the shear zone's dip-angle (< 15°), stable conditions cannot be assured, as the formation of the active wedge by progressive, localised fracturing within the rock mass resulted in stress conditions that surpassed the shear strength of the tectonic shear zone. At the same time, this implies that the driving forces will become smaller with increasing displacement as the active wedge slides down the S3 structures and lowers its potential energy. Kellerer-Pirklbauer et al. (2012) further found that circa 57,000 m^3 of rock fall debris from the MB has been deposited on the southwestern and north-eastern flanks of the MB ridge, further reducing the gravitational driving forces acting on the passive wedge, suggesting that the MB rockslide will come to calm. However, an ongoing creep of the rockslide debris must be expected, potentially strongly interacting with high-precipitation and snow-melt events.

Furthermore, the combined DEM-FDEM approach revealed important implications for numerical modelling. The asymmetric Voronoi approach was highly feasible in performing multi-stage, parametric numerical analyses and in recreating the initial failure geometry in remarkable agreement with field observations. However, the asymmetric Voronoi DEM fell short in developing larger displacements at the MB, as a rock bridge remained, exhibiting shear stress concentrations in the Voronoi elements (Fig. 18a). This resulted in interlocking and, consequently, in a premature stabilisation of the rockslide, as the Voronoi elements themselves cannot break but only deform in an elastic or elastoplastic manner. This is where the FDEM approach proved to be highly feasible, as the fractured zone developed in the same location where the DEM approach fell short in developing brittle fractures (Fig. 18b). This should be considered for any rock slope instability studies, as the displacement magnitude of rockslides may be underestimated thereby.

6. Conclusions

This study shows how fracture propagation can dominate over inherited rock mass structure even in strongly structurally preconditioned rockslides, highlighting the importance of adequately addressing brittle rock mass fracturing in rock slope stability studies and hazard assessment. A complementary numerical DEM (asymmetric Voronoi) and FDEM approach proved to be highly feasible in back-calculating the initial rock slope failures and carrying out parametric studies to investigate the role of rock mass fracturing in the evolution of two high-alpine rockslides. However, it is demonstrated that certain limitations arise from a solely DEM approach, which can potentially be overcome by applying FDEM. These implications should be treated with care in any rock slope stability studies, as neglecting rock mass fracturing could result in a faulty assessment of rock slope stability and displacement magnitudes. This was shown for the rockslides presented herein.

The 1,000,000 m^3 Rauhjoch (RJ) rockslide formed on a dip-slope composed of a rock mass with highly persistent, well-pronounced foliation layers. These foliation layers play a key role in the rockslide development. As these foliation layers do not daylight on the slope, a toe-breakout was crucial in initiating the rockslide, thereby decreasing the overall dip-angle of the basal detachment zone and reaching the daylight envelope of the pre-failure slope. After the toe-breakout, the rockslide developed retrogressively from the toe towards the peak. This was reproduced numerically in both DEM and FDEM approaches, demonstrating that despite the strong structural control, neglecting rock mass fracturing may result in a faulty perception of the kinematic feasibility for rock slope failure.

The rockslide on the Mittlerer Burgstall (MB) involves circa 670,000 m^3 and shows a compound rock sliding mechanism involving steep brittle structures at the head of the rockslide and a shallow-dipping tectonic shear zone at the rockslide foot. Rock mass fracturing was crucial for the compound rockslide initiation, especially in the transition zone from the active to the passive wedge. In the compound rockslide, the overall dip-angle of the basal detachment surface was increased, overcoming the frictional resistance of the tectonic shear zone, composed of a material containing chlorite and talc. This allowed to demonstrate how rock mass fracturing and the development of new macroscopic fractures can be crucial for initiating rock slope failure, even if the pre-existing structures already fulfil the geometrical conditions for rock slope failure.

Thus, our study demonstrates that fracture propagation in intensely foliated rock masses can overcome the inherited rock structure in controlling the mechanisms, evolution, and final failure of large rockslides.

CRediT authorship contribution statement

R. Gerstner: Visualization, Methodology, Formal analysis, Writing – original draft, Software, Investigation, Conceptualization. **A. Maschler:** Investigation, Writing – review & editing. **B. Schneider-Muntau:** Resources, Conceptualization, Writing – review & editing, Investigation. **F. Agliardi:** Supervision, Conceptualization, Writing – review & editing, Methodology. **M. Avian:** Resources, Investigation, Methodology. **M. Frießenbichler:** Methodology, Investigation. **C. Zangerl:** Supervision, Writing – review & editing, Conceptualization.

Declaration of competing interest

The authors declare that they have no known competing financial interests or personal relationships that could have appeared to influence the work reported in this paper.

Acknowledgements

We, the authors, would like to express our sincere gratitude to Maximilian Stauber from the University of Innsbruck for his work on the direct shear tests, Gerald Valentin from Land Salzburg and Volkmar Mair from Provinz Bozen/Südtirol for supporting this scientific research. Also, we would like to thank the ACRP14 - CAUTION - KR21KB0K00001 project team and the HADRIAN Doctoral School at BOKU University for their ongoing support.

Data availability

Data will be made available on request.

References

Agliardi, F., Crosta, G., Zanchi, A., 2001. Structural constraints on deep-seated slope deformation kinematics. Eng. Geol. 59 (1–2), 83–102. https://doi.org/10.1016/S0013-7952(00)00066-1.

Agliardi, F., Riva, F., Barbarano, M., Zanchetta, S., Scotti, R., Zanchi, A., 2019. Effects of tectonic structures and long-term seismicity on paraglacial giant slope deformations: Piz Dora (Switzerland). Eng. Geol. 263, 105353. https://doi.org/10.1016/j.enggeo.2019.105353.

Agliardi, F., Scuderi, M.M., Fusi, N., Collettini, C., 2020. Slow-to-fast transition of giant creeping rockslides modulated by undrained loading in basal shear zones. Nat. Commun. 11 (1), 1352. https://doi.org/10.1038/s41467-020-15093-3.

Amitrano, D., Helmstetter, A., 2006. Brittle creep, damage, and time to failure in rocks. J. Geophys. Res. Solid Earth 111 (B11). https://doi.org/10.1029/2005JB004252.

APCC, 2014. Österreichischer Sachstandsbericht Klimawandel 2014 (AAR14). Austrian Panel on Climate Change (APCC). V. d. Österreichischen & A. d. Wissenschaften. https://verlag.oeaw.ac.at/produkt/oesterreichischer-sachstandsbericht-klimawandel-2014.

Atkinson, B.K., 1984. Subcritical crack growth in geological materials. J. Geophys. Res. Solid Earth 89, 4077–4114. https://doi.org/10.1029/JB089iB06p04077.

Autonome Provinz Bozen, 2025. Natur, Landschaft und Raumentwicklung - Landeskartografie. https://natur-raum.provinz.bz.it/de/orthofotos-und-historische-luftbilder.

Avian, M., Kaufmann, V., Slupetzky, H., 2014. Photogrammetrische Auswertung des Bildfluges Pasterze 2003 (Projekt des Bundesministeriums für Wissenschaft und Forschung und des Hydrographischen Dienstes), Amt der Salzburger Landesregierung im Rahmen der Bund-Länder-Kooperation.

Brideau, M.-A., Yan, M., Stead, D., 2009. The role of tectonic damage and brittle rock fracture in the development of large rock slope failures. Geomorphology 103 (1), 30–49. https://doi.org/10.1016/j.geomorph.2008.04.010.

Bunkholt, H., Redfield, T., Osmundsen, P., Oppikofer, T., Hermanns, R., Dehls, J., 2012. Landslide processes in hard rock in Troms, Norway. In: Landslides and Engineered Slopes: Protecting Society through Improved Understanding. Taylor & Francis Group, London, pp. 855–861.

CARG, 2023. Erläuterungen zur Geologischen Karte von Italien im Maßstab 1:50.000 Blatt 006 St. Leonhard in Passaier (Carta Geologica D'Italia), Issue.

CARG, 2024. Geologische Karte 1:50.000 (CARG) - Blatt S. Leonard in Passeiertal. Piacenza Autonome Provinz Bozen.

Chigira, M., 1992. Long-term gravitational deformation of rocks by mass rock creep. Eng. Geol. 32 (3), 157–184. https://doi.org/10.1016/0013-7952(92)90043-X.

Conrad, O., Bechtel, B., Bock, M., Dietrich, H., Fischer, E., Gerlitz, L., Wehberg, J., Wichmann, V., Böhner, J., 2015. System for automated geoscientific analyses (SAGA) v. 2.1. 4. In: Geoscientific Model Development.

Cornelius, H.P., Clar, E., 1934. Geologische Karte des Großglocknergebietes 1:25.000. Geologische Bundesanstalt, Wien.

Donath, F.A., 1961. Experimental study of shear failure in anisotropic rocks. Geol. Soc. Am. Bull. 72 (6), 985–989.

Donati, D., Stead, D., Brideau, M.-A., Ghirotti, M., 2021. Using pre-failure and post-failure remote sensing data to constrain the three-dimensional numerical model of a large rock slope failure. Landslides 18 (3), 827–847. https://doi.org/10.1007/s10346-020-01552-x.

Eberhardt, E., Willenberg, H., Loew, S., Maurer, H., 2001. Active rockslides in Switzerland - understanding mechanisms and processes. In: Landslides - Causes, Impacts and Countermeasures, Davos, Switzerland.

Eberhardt, E., Stead, D., Coggan, J.S., 2004. Numerical analysis of initiation and progressive failure in natural rock slopes—the 1991 Randa rockslide. Int. J. Rock Mech. Min. Sci. 41 (1), 69–87. https://doi.org/10.1016/S1365-1609(03)00076-5.

Einstein, H.H., Veneziano, D., Baecher, G.B., O'Reilly, K.J., 1983. The effect of discontinuity persistence on rock slope stability. Int. J. Rock Mech. Min. Sci. Geomech. Abstr. 20 (5), 227–236. https://doi.org/10.1016/0148-9062(83)90003-7.

Elmo, D., Stead, D., 2010. An integrated numerical modelling–discrete fracture network approach applied to the characterisation of rock mass strength of naturally fractured pillars. Rock Mech. Rock. Eng. 43 (1), 3–19. https://doi.org/10.1007/s00603-009-0027-3.

Fey, C., Wichmann, V., 2017. Long-range terrestrial laser scanning for geomorphological change detection in alpine terrain - handling uncertainties. Earth Surf. Process. Landf. 42 (5), 789–802. https://doi.org/10.1002/esp.4022.

Fey, C., Rutzinger, M., Wichmann, V., Prager, C., Bremer, M., Zangerl, C., 2015. Deriving 3D displacement vectors from multi-temporal airborne laser scanning data for landslide activity analyses. GISci. Remote Sens. 52 (4), 437–461. https://doi.org/10.1080/15481603.2015.1045278.

Fischer, A., Seiser, B., Stocker Waldhuber, M., Mitterer, C., Abermann, J., 2015. Tracing glacier changes in Austria from the little ice age to the present using a lidar-based high-resolution glacier inventory in Austria. Cryosphere 9 (2), 753–766. https://doi.org/10.5194/tc-9-753-2015.

Geomechanica Inc, 2024. IRAZU 2D Tutorial Manual. In (Version 6.2).

Gerstner, R., Fey, C., Kuschel, E., Valentin, G., Voit, K., Zangerl, C., 2023. Polyphase rock slope failure controlled by pre-existing geological structures and rock bridges. Bull. Eng. Geol. Environ. 82 (9), 363. https://doi.org/10.1007/s10064-023-03382-2.

Gerstner, R., Fey, C., Kuschel, E., Lehner, F., Valentin, G., Voit, K., Zangerl, C., 2025. Insights into the evolution of a post-failure rock slope. Bull. Eng. Geol. Environ. 84 (5), 232. https://doi.org/10.1007/s10064-025-04249-4.

Gischig, V., Preisig, G., Eberhardt, E., 2016. Numerical investigation of seismically induced rock mass fatigue as a mechanism contributing to the progressive failure of deep-seated landslides. Rock Mech. Rock. Eng. 49 (6), 2457–2478. https://doi.org/10.1007/s00603-015-0821-z.

Glastonbury, J., Fell, R., 2010. Geotechnical characteristics of large rapid rock slides. Can. Geotech. J. 47 (1), 116–132.

Grämiger, L.M., Moore, J.R., Gischig, V.S., Ivy-Ochs, S., Loew, S., 2017. Beyond debuttressing: mechanics of paraglacial rock slope damage during repeat glacial cycles. J. Geophys. Res. Earth 122 (4), 1004–1036. https://doi.org/10.1002/2016JF003967.

Groß, P., Handy, M.R., John, T., Pestal, G., Pleuger, J., 2020. Crustal-scale sheath folding at HP conditions in an exhumed alpine subduction zone (Tauern Window, Eastern Alps). Tectonics 39 (2), e2019TC005942. https://doi.org/10.1029/2019TC005942.

Havaej, M., Wolter, A., Stead, D., Tuckey, Z., Lorig, L., Eberhardt, E., 2013. Incorporating brittle fracture into three-dimensional modelling of rock slopes Slope 2013. In: 2013 International Symposium on Slope Stability in Open Pit Mining and Civil Engineering, Perth. https://papers.acg.uwa.edu.au/p/1308_41_Havaej/.

Havaej, M., Stead, D., Eberhardt, E., Fisher, B.R., 2014. Characterization of bi-planar and ploughing failure mechanisms in footwall slopes using numerical modelling. Eng. Geol. 178, 109–120. https://doi.org/10.1016/j.enggeo.2014.06.003.

Hencher, S., Liao, Q., Monaghan, B., 1996. Modelling slope behaviour for open-pits. Trans. Inst. Min. Metall. A Min. Ind. 105, A37.

Höck, V., Pestal, G., 1994. Geologische Karte der Republik Österreich 1: 50000, Blatt 153, Großglockner (Geological Map of Austria 1: 50,000 Sheet 153, Großglockner). Geologische Bundesanstalt, Vienna.

Hungr, O., Leroueil, S., Picarelli, L., 2014. The Varnes classification of landslide types, an update. Landslides 11, 167–194. https://doi.org/10.1007/s10346-013-0436-y.

Itasca, 2016. PFC2D (Particle Flow Code in 2 Dimensions) Manual. Version 5. Itasca Consulting Group Inc, Minneapolis, MN.

Itasca, 2018. UDEC—Universal Distinct Element Code, Version 7.0, User's Manual. In (Version 7.0). Itasca Consulting Group.

Kellerer-Pirklbauer, A., Lieb, G.K., Avian, M., Carrivick, J., 2012. Climate change and rock fall events in high mountain areas: numerous and extensive rock falls in 2007 at Mittlerer Burgstall, Central Austria. Geogr. Ann. Ser. B 94 (1), 59–78.

Kemeny, J., 2005. Time-dependent drift degradation due to the progressive failure of rock bridges along discontinuities. Int. J. Rock Mech. Min. Sci. 42, 35–46. https://doi.org/10.1016/j.ijrmms.2004.07.001.

Klug, L., Froitzheim, N., 2022. Reuniting the Ötztal Nappe: the tectonic evolution of the Schneeberg complex. Int. J. Earth Sci. 111 (2), 525–542. https://doi.org/10.1007/s00531-021-02127-4.

Krautblatter, M., Funk, D., Günzel, F.K., 2013. Why permafrost rocks become unstable: a rock–ice-mechanical model in time and space. Earth Surf. Process. Landf. 38 (8), 876–887. https://doi.org/10.1002/esp.3374.

Lisjak, A., Grasselli, G., 2014. A review of discrete modeling techniques for fracturing processes in discontinuous rock masses. J. Rock Mech. Geotech. Eng. 6 (4), 301–314. https://doi.org/10.1016/j.jrmge.2013.12.007.
Lisjak, A., Grasselli, G., Vietor, T., 2014. Continuum–discontinuum analysis of failure mechanisms around unsupported circular excavations in anisotropic clay shales. Int. J. Rock Mech. Min. Sci. 65, 96–115. https://doi.org/10.1016/j.ijrmms.2013.10.006.
LLC A, 2022. Agisoft Metashape User Manual: Professional Edition. In (Version Version 1.8) [User Manuel]. https://www.agisoft.com/downloads/user-manuals/.
Maschler, A., 2022. Geologische Charakterisierung und Prozessanalyse der Felsgleitung an der Rauhjochspitze (Passeiertal, Südtirol). Master's Thesis. University of Natural Resources and Life Sciences, Vienna.
Paronuzzi, P., Bolla, A., 2022. In-depth field survey of a rockslide detachment surface to recognise the occurrence of gravity-induced cracking. Eng. Geol. 302, 106636. https://doi.org/10.1016/j.enggeo.2022.106636.
Passchier, C.W., Trouw, R.A., 2005. Microtectonics. Springer Berlin, Heidelberg. https://doi.org/10.1007/3-540-29359-0.
Pogrebiskii, M., Chernyshev, S.N., 1977. Determination of the permeability of the frozen fissured rock massif in the vicinity of the kolyma hydroelectric power station. US army cold regions research & engineering lab translation TL 634, 1–13.
Priest, S.D., 1993. Discontinuity analysis for rock. Engineering. https://doi.org/10.1007/978-94-011-1498-1.
Prochaska, A.B., Santi, P.M., Higgins, J.D., Cannon, S.H., 2008. Debris-flow runout predictions based on the average channel slope (ACS). Eng. Geol. 98 (1), 29–40. https://doi.org/10.1016/j.enggeo.2008.01.011.
Rechberger, C., Zangerl, C., 2022. Rock mass characterisation and distinct element modelling of a deep-seated rock slide influenced by glacier retreat. Eng. Geol. 300, 106584. https://doi.org/10.1016/j.enggeo.2022.106584.
Rechberger, C., Fey, C., Zangerl, C., 2021. Structural characterisation, internal deformation, and kinematics of an active deep-seated rock slide in a valley glacier retreat area. Eng. Geol. 286. https://doi.org/10.1016/j.enggeo.2021.106048.
Riva, F., Agliardi, F., Amitrano, D., Crosta, G.B., 2018. Damage-based time-dependent modeling of paraglacial to postglacial progressive failure of large rock slopes. J. Geophys. Res. Earth 123 (1), 124–141. https://doi.org/10.1002/2017JF004423.
Roberts, N., Evans, S., 2013. The gigantic Seymareh (Saidmarreh) rock avalanche, Zagros Fold–Thrust Belt, Iran. J. Geol. Soc. 170 (4), 685–700. https://doi.org/10.1144/jgs2012-090.
Rockfield, 2017. ELFEN Manual, Version 4,7.1. Rockfield Software Ltd. https://www.rockfieldglobal.com/software/elfen-forward-modelling/.
Rocscience, 2020. Dips 8.003 - Graphical and Statistical Analysis of Orientation Data (Software). https://www.rocscience.com/.
Scambos, T.A., Dutkiewicz, M.J., Wilson, J.C., Bindschadler, R.A., 1992. Application of image cross-correlation to the measurement of glacier velocity using satellite image data. Remote Sens. Environ. 42 (3), 177–186. https://doi.org/10.1016/0034-4257(92)90101-O.
Schmid, S.M., Fügenschuh, B., Kissling, E., Schuster, R., 2004. Tectonic map and overall architecture of the Alpine orogen. Eclogae Geol. Helv. 97, 93–117. https://doi.org/10.1007/s00015-004-1113-x.
Schmid, S.M., Scharf, A., Handy, M.R., Rosenberg, C.L., 2013. The Tauern Window (Eastern Alps, Austria): a new tectonic map, with cross-sections and a tectonometamorphic synthesis. Swiss J. Geosci. 106, 1–32. https://doi.org/10.1007/s00015-013-0123-y.
Simon, S., 1897. Oetzthal & Stubai - Blatt III - S. Gurgl [4 Karten: mehrfarbig; 62 x 50 cm]. [Innsbruck]. Deutscher u. Oesterreichischer Alpen-Verein. https://doi.org/10.3931/e-rara-38954.
Sölva, H., Grasemann, B., Thöni, M., Thiede, R., Habler, G., 2005. The Schneeberg normal fault zone: normal faulting associated with cretaceous SE-directed extrusion in the Eastern Alps (Italy/Austria). Tectonophysics 401 (3), 143–166. https://doi.org/10.1016/j.tecto.2005.02.005.
Spreafico, M.C., Cervi, F., Francioni, M., Stead, D., Borgatti, L., 2017. An investigation into the development of toppling at the edge of fractured rock plateaux using a numerical modelling approach. Geomorphology 288, 83–98. https://doi.org/10.1016/j.geomorph.2017.03.023.
Stead, D., Wolter, A., 2015. A critical review of rock slope failure mechanisms: the importance of structural geology. J. Struct. Geol. 74, 1–23. https://doi.org/10.1016/j.jsg.2015.02.002.
Strauhal, T., Zangerl, C., Fellin, W., Holzmann, M., Engl, D.A., Brandner, R., Tropper, P., Tessadri, R., 2017. Structure, mineralogy and geomechanical properties of shear zones of deep-seated rockslides in metamorphic rocks (Tyrol, Austria). Rock Mech. Rock. Eng. 50 (2), 419–438. https://doi.org/10.1007/s00603-016-1113-y.
Sun, L., Grasselli, G., Liu, Q., Aboayanah, K.R., Huang, S., Tang, X., 2025. Investigating the frost cracking mechanism and the related shallow alpine rockfall initiation process using three-dimensional FDEM. Eng. Geol. 348, 107960. https://doi.org/10.1016/j.enggeo.2025.107960.
Terzaghi, K., 1962. Stability of steep slopes on hard unweathered rock. Geotechnique 12, 251–270. https://doi.org/10.1680/geot.1962.12.4.251.
Thiele, S.T., Grose, L., Samsu, A., Micklethwaite, S., Vollgger, S.A., Cruden, A.R., 2017. Rapid, semi-automatic fracture and contact mapping for point clouds, images and geophysical data. Solid Earth 8 (6), 1241–1253. https://doi.org/10.5194/se-8-1241-2017.
Vick, L.M., Böhme, M., Rouyet, L., Bergh, S.G., Corner, G.D., Lauknes, T.R., 2020. Structurally controlled rock slope deformation in northern Norway. Landslides 17 (8), 1745–1776. https://doi.org/10.1007/s10346-020-01421-7.
Whittaker, B.N., Singh, R.N., Sun, G., 1992. Rock Fracture Mechanics. Principles, Design and Applications.
Wyllie, D.C., Mah, C., 2004. Rock Slope Engineering - Civil and Mining, 4th ed. Spon Press Taylor and Francis Group. https://doi.org/10.1201/9781315274980.
Yan, M., 2008. Numerical Modelling of Brittle Fracture and Step-Path Failure: From Laboratory to Rock Slope Scale.
Zangerl, C., Fey, C., Prager, C., 2019. Deformation characteristics and multi-slab formation of a deep-seated rock slide in a high alpine environment (Bliggspitze, Austria). Bull. Eng. Geol. Environ. 78 (8), 6111–6130. https://doi.org/10.1007/s10064-019-01516-z.
Zhang, X.-P., Wong, L.N.Y., Wang, S.-J., Han, G.-Y., 2011. Engineering properties of quartz mica schist. Eng. Geol. 121 (3), 135–149. https://doi.org/10.1016/j.enggeo.2011.04.020.
Zhou, X., Chen, J., 2019. Extended finite element simulation of step-path brittle failure in rock slopes with non-persistent en-echelon joints. Eng. Geol. 250, 65–88. https://doi.org/10.1016/j.enggeo.2019.01.012.
Zhou, Y., Zhao, X., 2024. Time-dependent degradation of sliding cohesion due to subcritical crack propagation and damage to rock bridge in rock slopes. Eng. Geol. 333, 107494. https://doi.org/10.1016/j.enggeo.2024.107494.